THESIS

2-

This is to certify that the

dissertation entitled

STUDY OF LIGHT NEUTRON RICH NUCLEI

presented by

MICHAEL FAUERBACK

has been accepted towards fulfillment
of the requirements for

___PhD___ degree in _PHISICS___

_____
Major professor

Date _March 24 1997_

0-12771

PLACE IN RETURN BOX to remove this checkout from your record.
TO AVOID FINES return on or before date due.

DATE DUE	DATE DUE	DATE DUE
JUL 1 7 2000		
AUG 2 8 0		

c:\circ\datedue.pm3-p.1

STUDY OF LIGHT NEUTRON RICH NUCLEI

by

MICHAEL FAUERBACH

A DISSERTATION

Submitted to
Michigan State University
in partial fulfilment of the requirements
for the Degree of

DOCTOR OF PHILOSOPHY

Department of Physics and Astronomy

1997

ABSTRACT

STUDY OF LIGHT NEUTRON RICH NUCLEI

By

Michael Fauerbach

One of the fundamental questions in nuclear physics is the exact location of the proton and neutron driplines. These driplines indicate the point at which nuclei are no longer stable against spontaneous particle emission. The predictions of the exact location of the driplines depend strongly on the model used, and the exact location of the neutron dripline is experimentally only known for the lightest elements. In the first part of the present work we will expand the knowledge of the exact location of the neutron dripline by searching for the nucleus ^{26}O, which has been the center of controversy for a long time, as different model calculations lead to varying results about its stability.

The second part of the present work discusses the Coulomb excitation of the one-neutron halo nucleus ^{11}Be on several secondary targets, ranging from ^{208}Pb to ^{9}Be. The different targets were used in order to investigate the various contributions on the cross section, which scale differently with A and Z. The nucleus ^{11}Be is the only known halo nucleus with a bound excited state, and only the $\frac{1}{2}^{+}$ ground state and the $\frac{1}{2}^{-}$ excited state are bound. Both bound states are neutron halo states with root-mean-square radii of approximately 7 fm. This fact makes ^{11}Be an excellent test case for Coulomb excitation with a radioactive beam.

To my family

ACKNOWLEDGEMENTS

Contents

List of Tables

List of Figures

Chapter 1

Introduction

1.1 Physics with Radioactive Nuclear Beams

One of the fastest growing – and most interesting – areas of nuclear physics is carried out with radioactive nuclear beams (RNBs). Up until recently, nuclear physics experiments were limited to beams and targets of stable or near stable isotopes. However, less than 300 isotopes are stable and can be found in nature, whereas predictions show that about 7,000 isotopes should be particle stable, which means their lifetime is long on a nuclear time scale, and they do not decay via spontaneous particle emission. The properties of these 'exotic' nuclei are of vital interest to many areas of nuclear structure and nuclear astrophysics. This is illustrated by Figure 1.1 in which the chart of nuclides is shown. The solid squares indicate the stable isotopes, and all isotopes between the two solid lines have been experimentally observed (February 1997). The dashed lines indicate the proton (B_p=0) and neutron (B_n=0) driplines according to the predictions of Myers and Swiatecki [Mye66], and the magic proton and neutron numbers are also indicated on the plot.

One of the fundamental questions in nuclear physics is the exact location of the so-called proton and neutron driplines. These driplines indicate the point at which nuclei are no longer stable against spontaneous particle emission. The predictions of
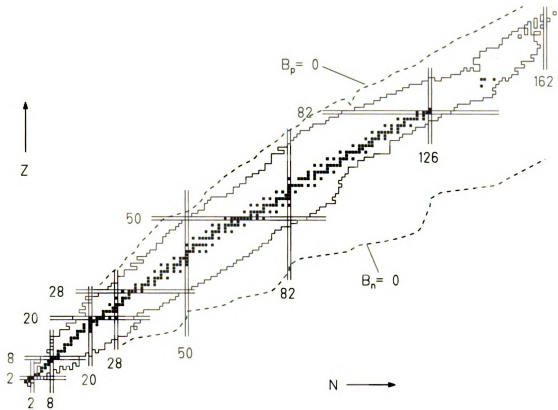
Figure 1.1: Chart of nuclides illustrating the limits of particle stability. The solid squares represent the stable isotopes, and the area between the two solid lines is the region of nuclei synthesized in the laboratory up to the present. The dashed lines indicate the proton and neutron driplines, according to Ref. [Mye66].

the exact location of the driplines depend strongly on the model used. Of course, these mass models all use information obtained from known isotopes. Information about the nuclear structure of isotopes farther away from stability has to be extrapolated from the available data taken closer to stability.

The onset of the proton dripline is determined by the balance between the attractive nuclear force and the repulsive Coulomb force between the protons in the nucleus. The repulsive character of the Coulomb force limits the extent of the proton-rich nuclei, so that the proton dripline is rather close to the valley of stability. This combined with the fact that the proton-rich nuclei are more easily accessible experimentally, leads to the fact that the proton dripline is mapped out to at least intermediate mass nuclei ($Z = 29$). On the neutron-rich side, on the other hand, the binding of the nuclei is basically limited by the filling of non-identical states in the nuclear potential well by neutrons. Therefore, the neutron dripline extends much further away from the valley of stability than the proton dripline. The exact location of the neutron dripline is only known experimentally for the lightest elements, and the theoretical predictions for heavier elements disagree, depending on the models used, by up to 5 to 10 mass units. Therefore, experimental studies to establish the limits of particle stability can yield important information.

Nuclei far away from stability are called 'exotic' not only because they do not exist in nature, but also because of the fact that they can exhibit new and 'exotic' behaviour. New decay modes, e.g. proton emission and β-delayed particle decay, have been observed. Other interesting topics include : the Gamow-Teller β-decay strength distribution, as well as the possibility of direct diproton decay for nuclei close to the proton dripline; 'superallowed' β-transitions observed for even neutron nuclei close to the neutron dripline, and many more. The nuclei close to the driplines are also of particular interest as they should show some unique properties due to their very small

one- or two-particle separation energies. This is especially true on the neutron-rich side, where the influence of the Coulomb force on the mean field is small. Very large nuclear matter radii have been found for several light neutron-rich nuclei and have been interpreted as evidence for a halo structure. A more detailed discussion about some properties of halo nuclei can be found in [Han95].

1.2 Production Mechanism

To perform experiments with radioactive beams, one first has to synthesize them in the laboratory. Several different techniques are employed to produce them, such as fusion-evaporation reactions, fission, as well as target- and projectile fragmentation. An overview about the different techniques can be found in the review articles by A.C. Mueller and B.M. Sherrill [Mue93] and H. Geissel, G. Münzenberg, and K. Riisager [Gei95] and references found therein. We will only briefly describe the technique of projectile fragmentation as it is employed for example at the National Superconduct-ing Cyclotron Laboratory (NSCL) at Michigan State University, and as it was used for the present work.

In 1947 Serber [Ser47] proposed the idea that peripheral high-energy heavy-ion reactions can be described by a two-step process in which each step takes place in a distinct time interval. The first step describes the violent collision between the constituents of the projectile and target nucleus. This step occurs on the order of 10^{-23}s and leads to so-called prefragments, which are excited and lose their excitation energy via the emission of particles (neutrons, protons, alphas, and sometimes even light clusters of particles) and γ-rays. This second, deexcitation step usually takes on the order of 10^{-18}s to 10^{-16}s, depending on the excitation energy. In Figure 1.2 one can see a schematic view of the process. A heavy ion projectile with mass A_P,

element number Z_P, and incident energy E_P interacts during a peripheral collision with a target nucleus with mass A_T and elemental number Z_T. The nucleons in the overlap zone of the two nuclei interact with each other, and in the most simple picture get sheared off the nuclei. The remnant of the projectile that was not involved in the collision – the so-called prefragment – travels with almost the beam velocity, loses its excitation energy via the evaporation of particles and γ-rays, and finally ends up as the observable fragment. For a more detailed microscopic description of the fragmentation process the reader may refer to [Fau92]. An overview of some of the experimental details involved in intermediate energy projectile fragmentation can be found in [Pfa96].
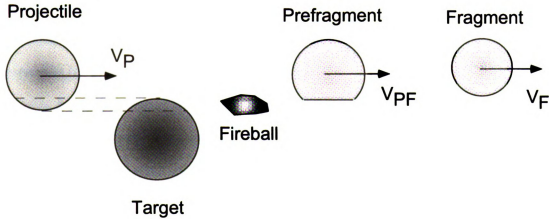
Figure 1.2: Schematic view of the projectile fragmentation process.

The different fragmentation products can be analyzed in fragment separators (see [She91, Mue93, Gei95], and Figure 2.4). The time to analyze the fragments is given by the flight time through the device, typically on the order of a couple of hundred nanoseconds. Therefore, in principle one can detect isotopes with a lifetime that is not significantly shorter than the analyzing time. This is a big advantage over Isotope Separation Online (ISOL) systems, which use target fragmentation induced by intense

proton or light ion (e.g. ^{12}C) beams. The production mechanism is similar to the one described above, however the radioactive isotopes produced have to be chemically released from the target, which takes typically on the order of milliseconds or more. Another advantage of projectile fragmentation is that the fragmentation products are forward focussed, travel with almost the same velocity as the incident beam, and are already ionized. Therefore, a radioactive ion beam of any element is readily available to impinge on a secondary reaction target, so that within limits – due to the lower available secondary beam intensities – similar experiments as with stable beams can now take place with radioactive beams. Again, this is an advantage over the ISOL facilities, where the radioactive ions have to be reaccelerated before they can be used for secondary experiments. However, the fact that the beams are produced at high incident beam energies for projectile fragmentation is not always advantageous. Most reactions of astrophysical interest take place at rather low energies which are not accessible by projectile fragmentation, in which the secondary beams typically have energies between several tens – or even several hundreds – of MeV/nucleon. ISOL facilities seem to be better suited for this kind of reaction. Therefore, the two methods of producing radioactive ion beams are complementary to each other.

1.3 Purpose of the present work

The ultimate purpose of the present work is to study light neutron rich nuclei. This thesis will concentrate on two different aspects of physics with radioactive beams. In the first generation of experiments with radioactive nuclear beams, the main purpose was to understand the production mechanisms involved in projectile fragmentation re-actions. Therefore detailed studies of momentum distributions and production yields were performed. These experiments are rather simple and straightforward but are still of great importance. As was mentioned earlier, the exact location of the neutron

dripline is only known for the lightest elements. Recent advances in technology that lead to an increase in the available primary beam intensities, enables one to push the limits ahead further. In the first part of the present work (Chapter 2) we will expand the knowledge of the exact location of the neutron dripline by searching for the nucleus ^{26}O. This nucleus has been the center of controversy for a long time, as different model calculations lead to varying results about its stability. Although a previous attempt to synthesize ^{26}O was not successful [Gui90], many people still speculated about its existence. In a recent paper by Z. Ren *et al.* [Ren95] for example, ^{26}O was described as a possible candidate for a four neutron halo nucleus.

Radioactive nuclear beams can of course also be used to perform secondary beam experiments. In this second generation of experiments, the radioactive nuclei interact with a secondary target, and depending on the experimental setup used, one can deduce a wide variety of nuclear structure information. These experiments require a much more sophisticated experimental setup than that used in the previously described first generation experiments. Now, the radioactive ions not only have to be produced and identified before they interact with the secondary target but also after, and often in coincidence with other particles and/or γ-radiation. In Chapter 3, we will describe a Coulomb excitation experiment with the one-neutron halo nucleus ^{11}Be on several secondary targets. During this experiment, the secondary beam was identified before it impinged on the secondary target, and the scattered particles were measured in coincidence with the emitted γ-rays. The nucleus ^{11}Be is the only known halo nucleus with a bound excited state; both the $\frac{1}{2}^{+}$ ground state and the $\frac{1}{2}^{-}$ excited state are bound. Both bound states are neutron halo states with root-mean-square radii of approximately 7 fm. This fact makes ^{11}Be an excellent test case for Coulomb excitation with a radioactive beam. There is also the possibility that more subtle effects will appear when the known lifetime of the first excited state is compared with cross

sections for inelastic nuclear scattering because (a) the Coulomb transition amplitude approaches unity at small impact parameters so that first-order perturbation theory, which is usually employed to describe Coulomb excitation, may no longer be valid, and (b) the extended halo wave functions may lead to nuclear excitation well beyond distances normally considered safe in Coulomb excitation experiments. However, the first Coulomb excitation experiment [Ann95], in which a 45 MeV/nucleon ^{11}Be beam bombarded a lead target, produced an excitation cross section of only 40% of the expected value for pure Coulomb excitation at this energy. This reduction is much larger than what could be reasonably expected from higher-order effects (calculated to be on the order of 10-20% [Ann95, Typ95, Kid96, Ber95]). In chapter 3, the results from our measurement on various targets will be discussed and compared to previous experimental data as well as to some theoretical predictions.

Chapter 2

The Search for ^{26}O

2.1 Motivation and Introduction

The exact location of the boundaries of particle stability - the so called driplines - are interesting from an experimental as well as from a theoretical standpoint. Many theoretical models, both macroscopic and microscopic, predict the ground state masses as well as the one- and two-particle separation energies, and therefore they also predict the driplines locations. The exact location of the neutron dripline is only known experimentally for the lightest elements, and, therefore, experimental studies to establish the limits of particle stability remain important. The nuclei close to the driplines are also of particular interest as they should show unique properties which are due to their very small one- or two-particle separation energies. This is especially true on the neutron-rich side, where the influence of the Coulomb force on the mean field is small. As an example, ^{11}Be has a very large nuclear matter radius that has been interpreted as evidence for a halo structure. It is expected that many more of these one- and two-neutron halo nuclei will be found as one approaches the limits of particle stability. In chapter 3, a discussion of some more detailed properties of the one neutron halo nucleus ^{11}Be is presented.

Some disagreements, particularly in the sodium region, between the experimen-

tally determined values and the theoretical estimates for the binding energies of the most neutron-rich isotopes have been noted by several authors [Wou88, Gui90]. With the use of large scale computer codes the disagreement has lessened in recent years although there are still several regions where the models do not agree with the experimental findings or with each other. The predictions of several models for the particle stability of ^{26}O can be summarized in terms of the binding energy curves for oxygen isotopes shown in Figure 2.1. The experimental data (solid circles) are compared with several predictions: the global prediction of Möller and Nix [Möl88] (MN) and two different shell-model calculations, labeled as W-WBMB and SDPOTA. W refers to Wildenthal's USD interaction [Wil84] obtained from a fit of the two-body matrix elements to binding energy and excitation energy data in the $0s1d$ shell (N,Z=8,20). SDPOTA [Bro88] is a more recent interaction obtained from a fit of density-dependent one-boson exchange potential strengths to the same set of energy data. The W interaction has effectively 47 parameters whereas SDPOTA is more constrained with 14 potential strength and three single-particle energy parameters. WBMB is an addition and extension of W into the fp shell [Wab90]. Both W and SDPOTA do about equally well in reproducing the known experimental binding energies of the oxygen isotopes.

The region close to the dripline is very sensitive to small differences in the binding energy since only a very small change in binding energy can determine whether a nucleus decays via β-decay or by spontaneous particle emission. Therefore, the location of the driplines is a stringent test for mass models and provides a good way to judge whether a particular model can be used to extrapolate away from stability. The global model of Möller and Nix predicts ^{26}O and even the doubly magic nucleus ^{28}O to be stable, while the global systematics by Audi and Wapstra [Aud93] predict ^{24}O as the heaviest bound oxygen isotope with ^{26}O unbound by 50 keV. The W -
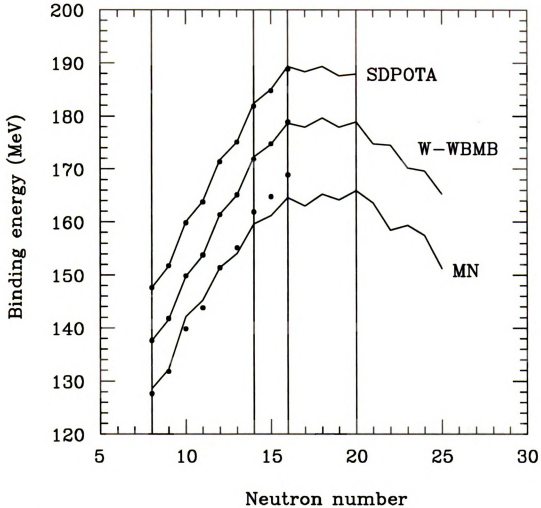
Figure 2.1: Measured binding energies of the ground states of oxygen isotopes (solid circles) compared to several model predictions (solid lines). For display purposes 10 MeV has been added to the W - WBMB comparison and 20 MeV to the SDPOTA comparison. The vertical lines indicate the filling of the $d_{5/2}$, $s_{1/2}$, and $d_{3/2}$ neutron orbits, respectively.

WBMB calculations also predict ^{26}O to be bound by about 1 MeV. The SDPOTA calculation, on the other hand, predicts ^{26}O to be unbound, but only by 20 keV. These differences are an indication of the rather large model dependence which exists in the theoretical extrapolation to the most exotic nuclei. In the case of the oxygen isotopes, the shell-model predictions rely on assumptions in the calculations which cannot be tested with known experimental data beyond ^{24}O. The odd-even nuclei $^{25,27}O$ are known to be unbound against one neutron decay [Aud93], in agreement with all of the model calculations.

The difficulty of predicting the binding energies of the heaviest oxygen isotopes, for both global- and shell-model calculations, can be easily understood in the simple j-j coupling limit. In Figure 2.2 the effective neutron separation energy (S_n) is shown as a function of neutron number. As can be clearly seen, S_n changes slowly with neutron number due to the relatively weak average interaction between the valence neutrons. Between N=8 and N=14, the neutrons fill the $d_{5/2}$ orbit, which is bound by about 4 MeV. This, together with the attractive pairing energy, provides the sharp increase in binding energy observed between N=8 and N=14. At N=15 and N=16 the neutrons fill the $s_{1/2}$ orbit which is less bound than the $d_{5/2}$. Thus one sees a smaller increase in the binding energy at this point. From N=16 up to N=20 the neutrons fill the $d_{3/2}$ orbit which has close to zero binding energy, and the total binding energy curve becomes flat. This slow variation in separation energy with the neutron number leads to difficulty in predicting whether a nucleus is bound or unbound. Beyond N=20 the neutrons have to go into the next major shell (pf orbits) which are unbound, hence the binding energy curve decreases beyond this point.

Figure 2.3 shows the two-neutron separation energies for the known isotopes in this region from the compilation of Audi and Wapstra [Aud93]. As clearly shown on this figure, all the elements near oxygen have several bound isotopes with two-
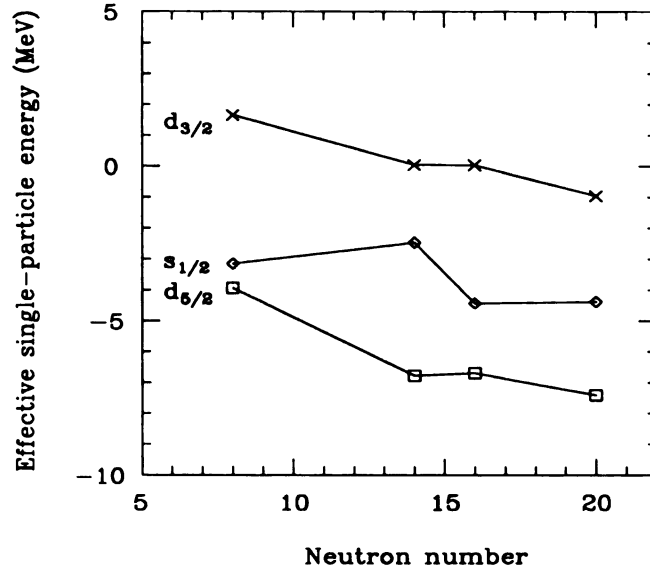
Figure 2.2: The effective neutron separation energy as a function of neutron number according to the shell-model calculations.

neutron separation energies that are much smaller than that of ^{24}O. The heaviest experimentally-known oxygen isotope is ^{24}O, and a previous attempt to synthesize ^{26}O using a ^{48}Ca beam was not successful [Gui90]. In the present work a new investigation of the particle stability of ^{26}O was carried out with greater sensitivity than that previously employed. This was possible due to the unique features given by the combination of the K1200/A1200, with the available high primary beam intensities, and the large acceptance of the A1200 for the rigid fragments.

2.2 Experimental Apparatus and Analysis

In the following the experimental apparatus used will be described along with the analysis procedures employed during the search for the very neutron-rich nucleus ^{26}O.

Figure 2.3: Two-neutron separation energies for various light isotopes as given by Ref. [Aud93]. The solid circles indicate measured values whereas the open circles show estimates from systematics for isotopes that are known to exist, but for which no direct mass measurements have been performed.

2.2.1 The A1200 Fragment Separator

A 90 MeV/nucleon ^{40}Ar beam from the K1200 cyclotron at the National Superconducting Cyclotron Laboratory at Michigan State University irradiated a 190 $\frac{mg}{cm^2}$ ^{9}Be target located at the medium acceptance target position of the A1200 fragment separator [She91]. The target thickness was chosen to optimize the production rate of the heavy oxygen fragments. The average beam intensity – using the superconducting ECR ion source – was about 20 particle nanoamps (pnA), which corresponds to approximately $1.25 \cdot 10^{11}$ particles per second (pps). The angular acceptances of the A1200 were ± 10 mrad in θ and ± 20 mrad in ϕ, centered around 0°. The momentum acceptance of the A1200 was set to the maximum of $\Delta p/p = \pm 1.5\%$. A schematic layout of the A1200 is shown in Figure 2.4.

In order to map out the (parallel) momentum distributions of the fragmentation

A1200 Radioactive Beam Facility
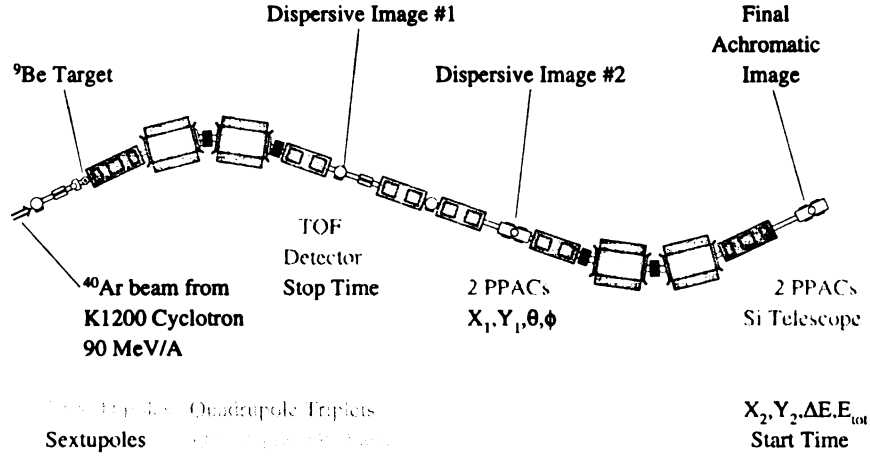
Figure 2.4: Schematic layout of the A1200 fragment separator.

products and to provide information about the production yields (see Ref. [Pfa95] for details), the magnetic rigidity of the separator was varied in overlapping steps over the range $B\rho = 2.96$ to 4.31 Tm. The relative beam current was monitored continuously by four small PIN diodes mounted around the target position to normalize data obtained at different magnetic rigidity settings. A small irreproducibility in the absolute beam current was found in the offline analysis. Therefore, a new magnetically shielded Faraday cup was built, and the beam intensity was carefully measured in subsequent short runs along with the yields of a few products. The cross sections for these products were calculated and used to renormalize the relative cross sections determined in the long experiment. In Figure 2.5 a schematic view of the new Faraday cup is shown. Two strong permanent magnets were glued to the sides to prevent secondary electrons from escaping.

The momentum distributions of the lighter oxygen isotopes were monitored online

so that the optimum separator setting for ^{26}O could be inferred without reference to any model calculations, an improvement over the previous experiment. Once the optimum setting was determined, an energy loss degrader (^{9}Be, 47 $\frac{mg}{cm}^2$) was inserted at the intermediate focal plane of the A1200 to cut down the range of atomic numbers of the fragments reaching the final focus. The fact that ^{26}O fragments would be centered at the intermediate image and the final focus of the A1200 was also verified online by measuring the positions of ^{19}C and ^{20}C fragments (which span ^{26}O in A/Q) at the intermediate focus and by measuring the energy loss of all the fragments versus their position at the final focus.

2.2.2   Detector Setup

The experiment used a standard detector setup for the A1200 fragment separator. The time of flight for each particle was measured over the 14 m flight path between a 8 $\frac{mg}{cm^2}$ thick plastic scintillator (BC404) located at the first dispersive image and the time pick-off signal from a totally depleted surface barrier semiconductor detector located at the focal plane of the A1200. The position and angle of the reaction products were measured at both the second dispersive image and at the focal plane with two pairs of x-y position sensitive parallel-plate avalanche counters (PPAC's) [Swa94], separated by approximately 40 cm. Combining the position measurement at the second dispersive image of the separator with NMR measurements of the A1200 dipole fields provided us with information about the magnetic rigidity (Bρ) of each particle. The magnetic rigidity is linearly related to its momentum (p) via the relation:

$$B\rho = \frac{p}{Q} = \frac{A\beta\gamma m_0 c}{Q} \qquad (2.1)$$

where Q is the particle charge, c is the speed of light, β and γ are the usual relativistic
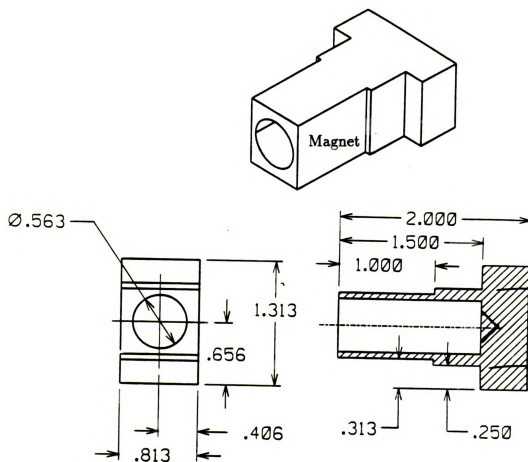
Figure 2.5: Schematic view of the magnetically shielded Faraday cup. The permanent magnets are located on both sides at the front of the Faraday cup, as indicated in the plot. All units are given in inches.

factors ($\beta = \frac{v}{c}$, $\gamma = \frac{1}{\sqrt{1-\beta^2}}$), A is the fragment mass number, and m_0 is the unified atomic mass number ($m_0 \approx 931.5\frac{MeV}{c^2}$). The reaction products that reached the A1200 focal plane were implanted into a four-element silicon detector telescope. The telescope consisted of two thin (100 and 75 μm) ΔE and two thicker (500 and 1000 μm) E detectors, each with a 300 mm^2 active area. All detectors were totally depleted surface barrier detectors, and were cooled to below +10° C to reduce thermal noise.

2.2.3 Electronic Setup

The standard, permanent A1200 electronics configuration was used for this experiment. A schematic view of the electronic setup is shown in Figure 2.6.

Thirty signals were read by the front end computer for each event trigger. The signals in detail were, a charge sensing ADC (QDC) and a TDC signal for the image #1 start detector; an ADC signal from the TAC measuring the flight time from the start detector to the ΔE1 detector; an ADC signal from the TAC measuring the time between the cyclotron RF and ΔE1; one TDC signal and four ADC signals (up, down, left, right) from each of the four PPAC detectors; an ADC and TDC signal from ΔE1 and ADC signals from the other silicon detectors. The master gate was constructed from a valid signal in the fourth silicon detector and a NOT BUSY signal from the front end CPU. We used the fourth silicon detector, not the usual condition of good signals in the first two silicon detectors for the mastergate, to enhance our sensitivity for low-Z isotopes. The data acquisition system, for both hardware and software, was the standard NSCL data acquisition system [Fox89]. The data were written on 8 mm tapes.
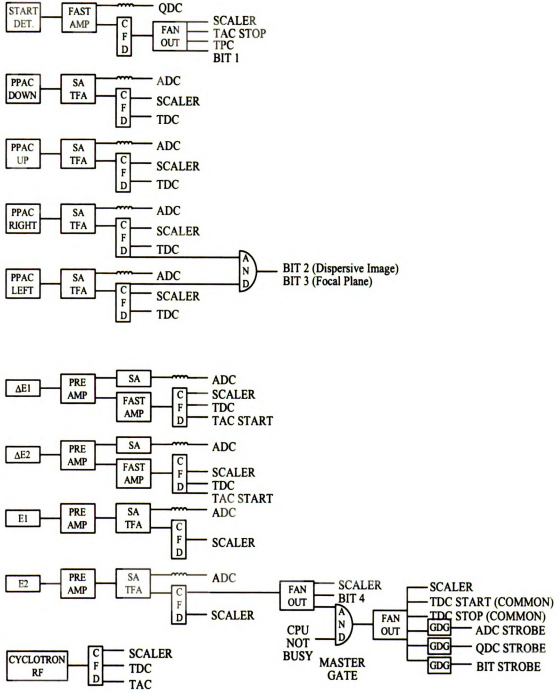
Figure 2.6: A schematic diagram of the electronic setup.

2.2.4 Isotope Identification

By transporting the primary beam through the production target and recording its horizontal position as a function of the magnetic rigidity, one is able to establish the rigidity calibration of the device. This is necessary in order to calculate the exact flight path of each fragment through the A1200 fragment separator on an event-by-event basis. The linear relationship between the magnetic rigidity and the horizontal (x) position at the second dispersive image of the A1200 fragment separator is shown in Figure 2.7. The open points represent the experimental data, and the solid line shows the linear fit to the data.
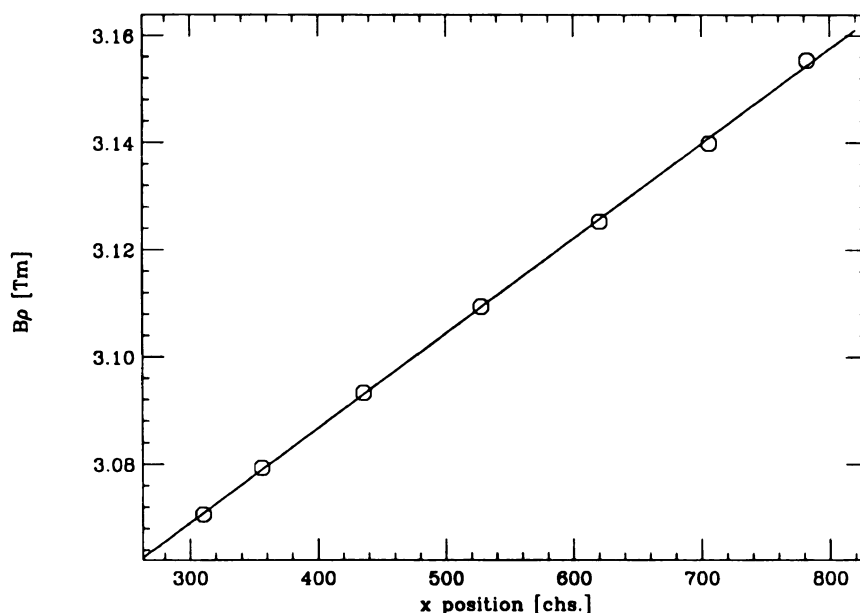
Figure 2.7: Magnetic rigidity versus the horizontal position at the dispersive image #2. The open circles represent the data, and the solid line is a linear fit to the data.

The initial isotope identification was performed by setting the magnetic rigidity of the A1200 about 3% higher than that of the primary beam through the production target. This way, the primary beam and lighter fragments could be detected simultaneously for unambiguous identification of the atomic number (Z). In a two

dimensional display of the energy loss (ΔE) versus the time-of-flight (TOF) the different elements form well separated bands. Individual isotopes are well separated in the same figure as is shown in Figure 2.8. The N = Z line as well as several of the isotopic bands are indicated in Figure 2.8. The isotope identification was independently verified by the absence of unbound or extremely short lived isotopes, like ^{8}Be.

An energy calibration for each silicon detector was obtained by comparison to the calculated amount of energy deposited in each detector, using the formalism given in Ref. [Hub89], to the observed ADC channel for various fragments. The total kinetic energy (TKE) deposited is then determined by summing up the energy loss in all four silicon detectors. The time-of-flight of the fragments was calibrated in a similar manner, by comparing the calculated TOF to the observed TDC channel. Figure 2.9 shows the energy and time calibrations obtained for the various detectors.

The simultaneous measurements of ΔE-E, the magnetic rigidity, and the time-of-flight for each particle provides an unambiguous identification of the atomic number (Z), charge state (Q) and mass of the produced fragments (A), via the following relationships :

$$Z = a + b\sqrt{\Delta E(\gamma - 1)} \tag{2.2}$$

$$Q = \frac{3.105Tm}{931.5MeV} * \frac{TKE * B\rho}{B\rho(\gamma - 1)} \tag{2.3}$$

$$A = \frac{Q * B\rho}{\beta\gamma * 3.105Tm} \tag{2.4}$$

Here, a and b are constants determined for each silicon detector, and β and γ are the usual relativistic factors ($\beta = \frac{v}{c}$, $\gamma = \frac{1}{\sqrt{1-\beta^2}}$), determined from the TOF of the fragment.

The combination of the high primary beam energy and the low atomic number of
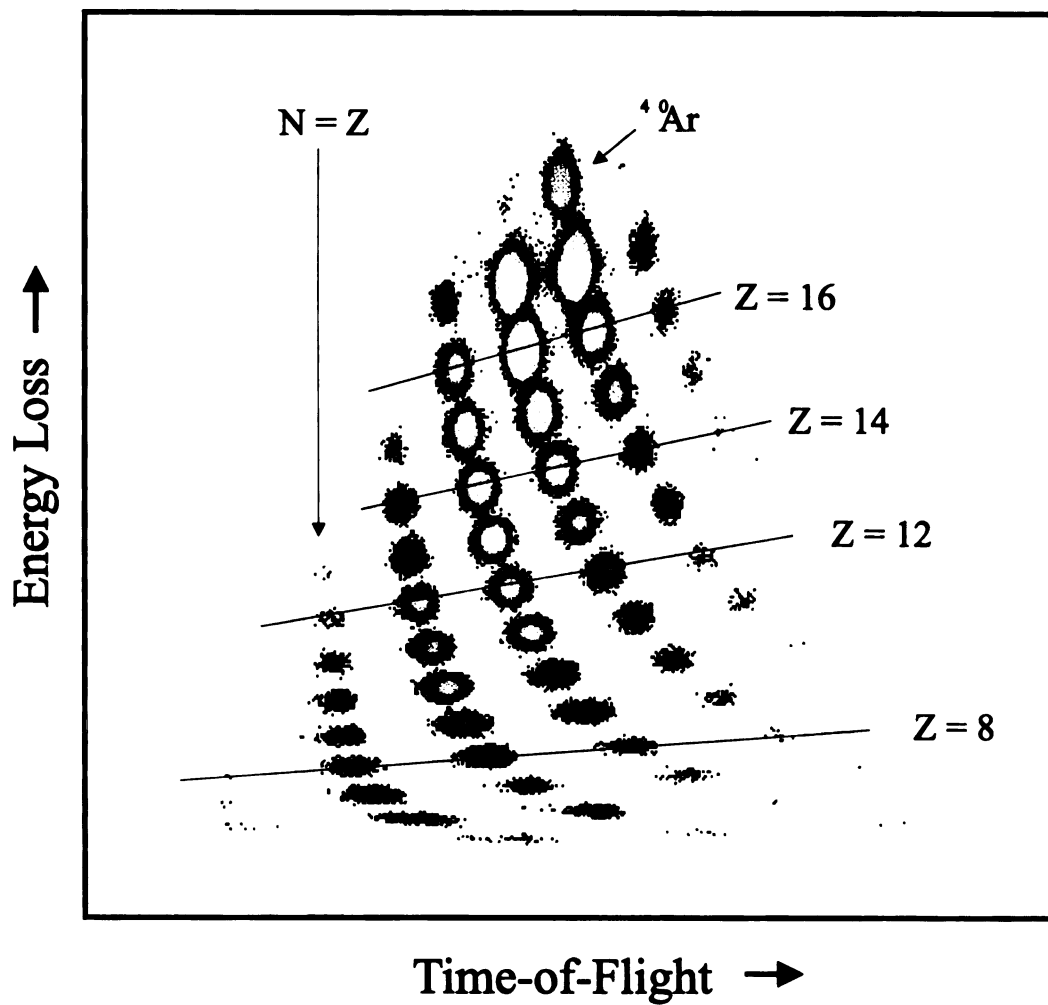
Figure 2.8: Energy loss versus time-of-flight as observed during the experiment.
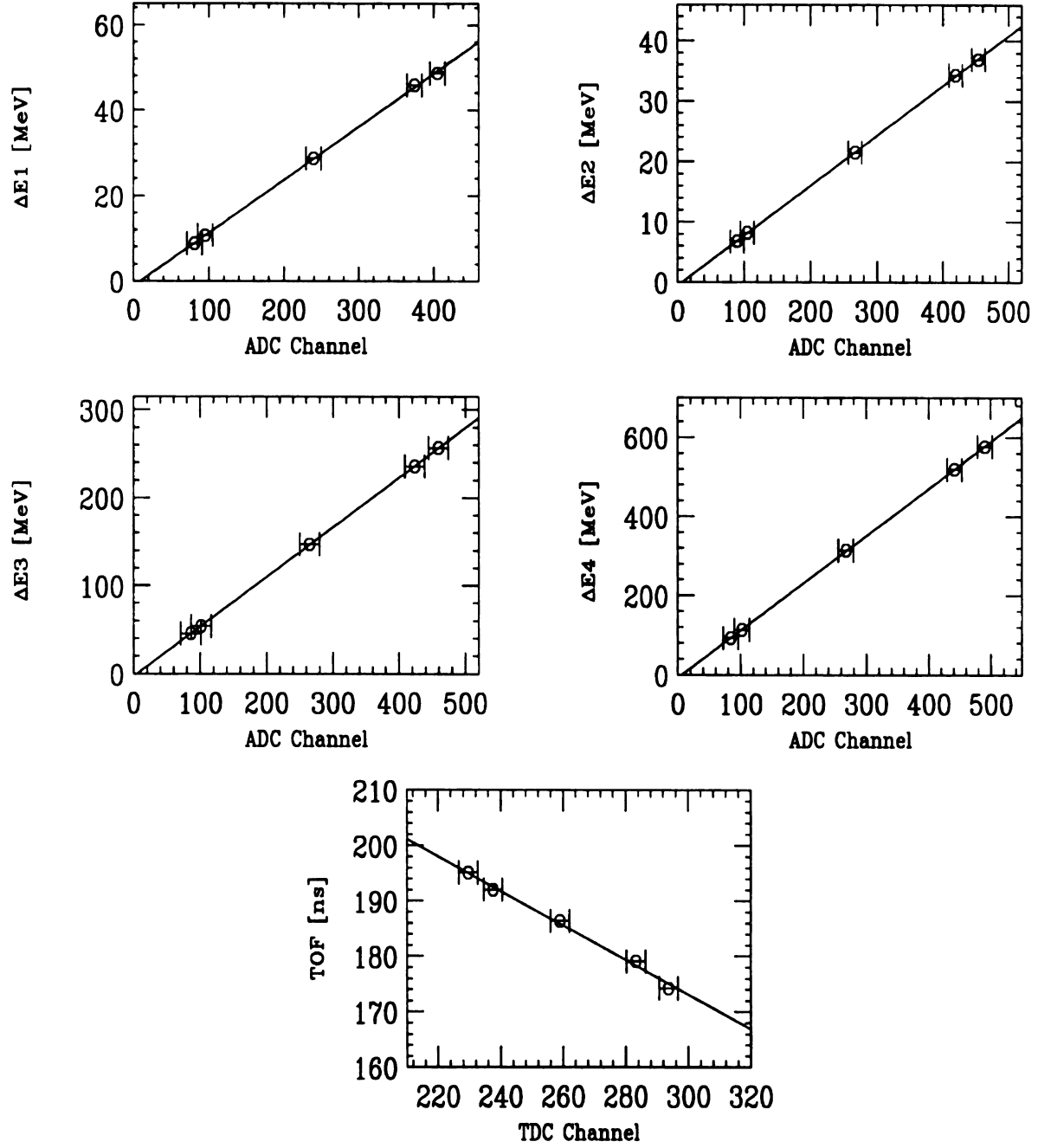
Figure 2.9: Energy and time calibrations for the detectors used. The open circles with the error bars represent the experimental data, and the solid lines show the linear fit used to calibrate the data.

the fragments assures that we only observe fully stripped fragments. A calculation, using the code INTENSITY [Win92], predicts the ratio of the fully stripped primary beam to the hydrogen-like primary beam after the production target to be about 10^{10} to 1. This fact was verified during the off-line analysis. Unfortunately, one of the silicon detectors ($\Delta E3$) was radiation damaged during this experiment, and as both its absolute efficiency and its energy resolution were deteriorating, it had to be neglected from further analysis. Therefore, we were not able to use the above formalism to determine Q, and A for the latter part of the measurement. However, as is shown in Figure 2.8 the isotopic separation in the two-dimensional ΔE versus TOF plot is very good and did not rely on the damaged detector. Therefore the production yields of the various fragments could be obtained from this plot. It should be noted again that this was possible because it was determined that all fragments were fully stripped.

2.3 Experimental Results and Discussion

The main objective of the experiment was to determine whether ^{26}O is particle bound. To make this determination, the momentum distributions of many neutron-rich fragments were carefully determined. This information was then used to determine production cross sections of these fragments and to find the optimum separator setting to observe ^{26}O. The results of these yield measurements will be discussed first and compared to the predictions of a semi-empirical parameterization [Süm90].

2.3.1 Momentum Distributions and Fragmentation Cross Sections

The momentum distributions of eight different oxygen isotopes in the range from ^{17}O to ^{24}O from the fragmentation of ^{40}Ar are shown in Figure 2.10. Notice that these

distributions span approximately seven orders of magnitude in relative production yield. As can be seen in Figure 2.10, the momentum distributions of the oxygen fragments are well described by Gaussian functions.

The widths of the individual momentum distributions were obtained from fitting Gaussian functions to the data. In Figure 2.3.1 we compare the measured momentum widths for various fragments (symbols) as a function of mass loss, to the formalism developed by Goldhaber [Gol74] (solid line). The dashed lines connect different isotopes (of the same element) and are only drawn to guide the eye. The Goldhaber model is an independent particle model which is based on the assumption that a nucleus can be described by a Fermi gas made up of independent nucleons. In the projectile rest frame the net momentum of the projectile is zero. The sudden removal of several nucleons, each moving with a mean momentum $< p >$ inside the projectile nucleus, results in a Gaussian recoil momentum distribution of the fragments. The width of this distribution in the projectile rest frame is given by the expression :

$$\sigma_\| = \sigma_0 \sqrt{\frac{A_F(A_P - A_F)}{A_P - 1}} \tag{2.5}$$

where $A_{P,F}$ denotes the mass of the projectile and fragment respectively. The reduced width σ_0 is the mean quadratic deviation of the momentum projected on one spatial dimension. Assuming that the width of the momentum distribution is the same in all three spatial dimension, one can calculate σ_0 as follows :

$$\sigma_0 = \frac{1}{\sqrt{3}} < p > \tag{2.6}$$

where $< p >$ is, as mentioned earlier, the mean momentum of the nucleons. This
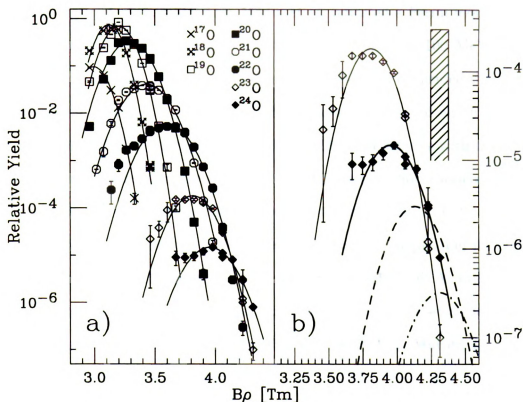
Figure 2.10: a) Measured relative production yield as a function of the magnetic rigidity, which is linearly related to the fragment momentum, for eight different oxygen isotopes ranging from ^{17}O to ^{24}O. The solid lines are Gaussian fits to the data. b) An expanded version showing only the measured values for ^{23,24}O. The dashed line indicates the expected momentum distribution for ^{25}O, which is unbound against one neutron decay. The dash-dotted line shows the expected momentum distribution for ^{26}O, and the hatched area shows the acceptance of the A1200 at one specific setting (see text for details).

mean momentum can be expressed in terms of the Fermi momentum (p_F) as :

$$< p >= \sqrt{\frac{3}{5}} p_F \qquad (2.7)$$

The Fermi momentum of the nucleons inside the nucleus has been determined previously by quasi-elastic electron scattering. Moniz *et al.* reported a Fermi momentum of $p_F \approx 230$ MeV/c for ^{40}Ar, leading to a reduced width of $\sigma_0 \approx 100$ MeV/c. A comparison to experimental data taken by Viyogi *et al.* [Viy79], confirmed the functional form given by equation 2.5. However, the value of the reduced width σ_0 had to be decreased to 90 MeV/c to reproduce the data. This discrepancy with the simple Fermi-gas model assumption has lead to several theoretical efforts which discuss possible causes for the narrowing of the observed momentum width. G.F. Bertsch [Ber81] for example pointed out the importance of the Pauli principle, and its effect on the momentum width. Hüfner and Nemes [Hüf81], as well as W.A. Friedmann [Fri83], use a geometric approach to take into account the fact that most nucleons are removed from the periphery of the nucleus. The articles by M.J. Murphy [Mur84], and H.H Gan *et al.* [Gan90] take into account that the nucleons that are not removed have to be bound in the fragment, which also introduces a reduction in σ_0.

As can be clearly seen in Figure 2.3.1, the measured momentum widths vary widely, and the heaviest observed isotope of a given element chain has the largest width. This is in contradiction to the Goldhaber model, which predicts that the width is only a function of mass loss. However, one can understand this behavior easily as being due to the target thickness effect. Since the main objective of the present experiment was to produce a very exotic nucleus, a relatively thick target was used to optimize the production rate of this nucleus. Dufour *et al.* [Duf86] have shown that the target thickness introduces an increase in the width of the momentum

distribution due to the difference in the energy lost by the projectile and that by the fragment in the target material. In the extreme case in which the fragment is produced at either the front or the back of the target, the differential energy loss creates an almost rectangular momentum distribution, the width of which increases in proportion to the target thickness. The width (σ_T) introduced by the target thickness can be parameterized as follows :

$$\sigma_T = c_T(\frac{Z_p^2}{A_P} - \frac{Z_F^2}{A_F}) \tag{2.8}$$

where c_T is a target specific constant, and $Z_{P,F}, A_{P,F}$ denote the atomic charge and the mass of the projectile or the observed fragment respectively. Equation 2.8 explains the observed behaviour of the increasing momentum width for the heaviest observed isotope of each element chain and shows that this effect is due to the thick production target used. In principle the two different components can be separated to give a nuclear reaction momentum width. However, since the unwanted effect from the target thickness was so large in the present case, the nuclear reaction widths were not deconvoluted. For similar reasons, we did not analyse the momentum shift of the fragments, as was done in Ref. [Pfa95].

Because the production cross sections are expected to change very little over the energy range spanned by the target thickness, the production cross sections were calculated and compared to the semi-empirical parameterization (EPAX) by Sümmerer, et al. [Süm90]. The absolute isotopic cross sections were obtained by integrating the fitted Gaussian distributions over momentum and normalizing the results by the incoming particle flux and the acceptance of the A1200. The incoming particle flux was measured between runs with a Faraday cup, and the beam current was monitored during the run using four PIN diodes mounted around the target position. The
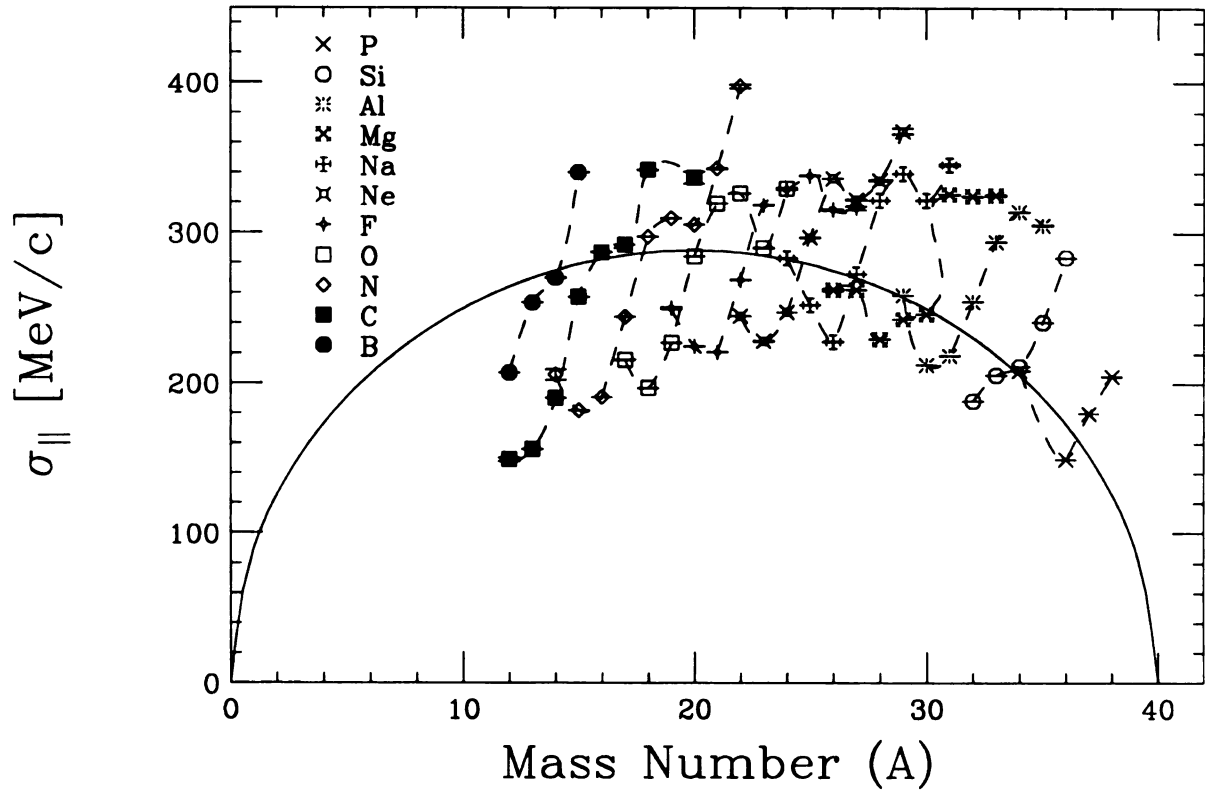
Figure 2.11: Measured parallel momentum width as a function of fragment mass. The solid line represents the predictions of the Goldhaber model, using $\sigma_0 = 90$ MeV/c.

acceptance for each individual isotope was calculated with the code LISE [Baz97].

The absolute production cross sections for 72 neutron-rich isotopes ranging from ^{11}B to ^{38}P were determined and are shown in Figure 2.12. The overall agreement between the measured data and predictions of the semi-empirical formula EPAX is good. However, slight deviations between the measured and predicted cross sections are present. In Figure 2.13, the cross sections for the oxygen isotopes are shown in more detail. Again, the overall agreement between the experimental data and the prediction is good although the measured cross sections indicate a slightly different functional form for the isotopic yield than that used by EPAX. A similar trend can be seen in Figure 2.12 for all isotopes with $Z < 12$. These, and other new data for light residues from fragmentation reactions could be used to refit the parameters of the EPAX formula to provide even better predictions of the cross sections.

The extrapolation of the expected counting rate for ^{26}O from the cross sections of the lighter oxygen isotopes is indicated in Figure 2.13. The EPAX prediction is shown by the solid line. However, due to the systematic difference mentioned above, a simple exponential fit to the most neutron-rich oxygen fragments was also used. Even though the curves have clearly different shapes, they predict a similar order of magnitude for the cross sections for ^{26}O, namely 2.43 nb (EPAX) and 1.07 nb (exponential fit).

2.3.2 The Search for ^{26}O

The carefully selected setting of the A1200 during the search for ^{26}O is indicated in Figure 2.10 by the hatched area, that corresponds to the momentum acceptance of the A1200 during the long run. After 36 hours of data collection at this one setting, 2132 events were identified as ^{24}O – approximately an order of magnitude more than the previous experiment [Gui90] – without a single event that could be attributed to
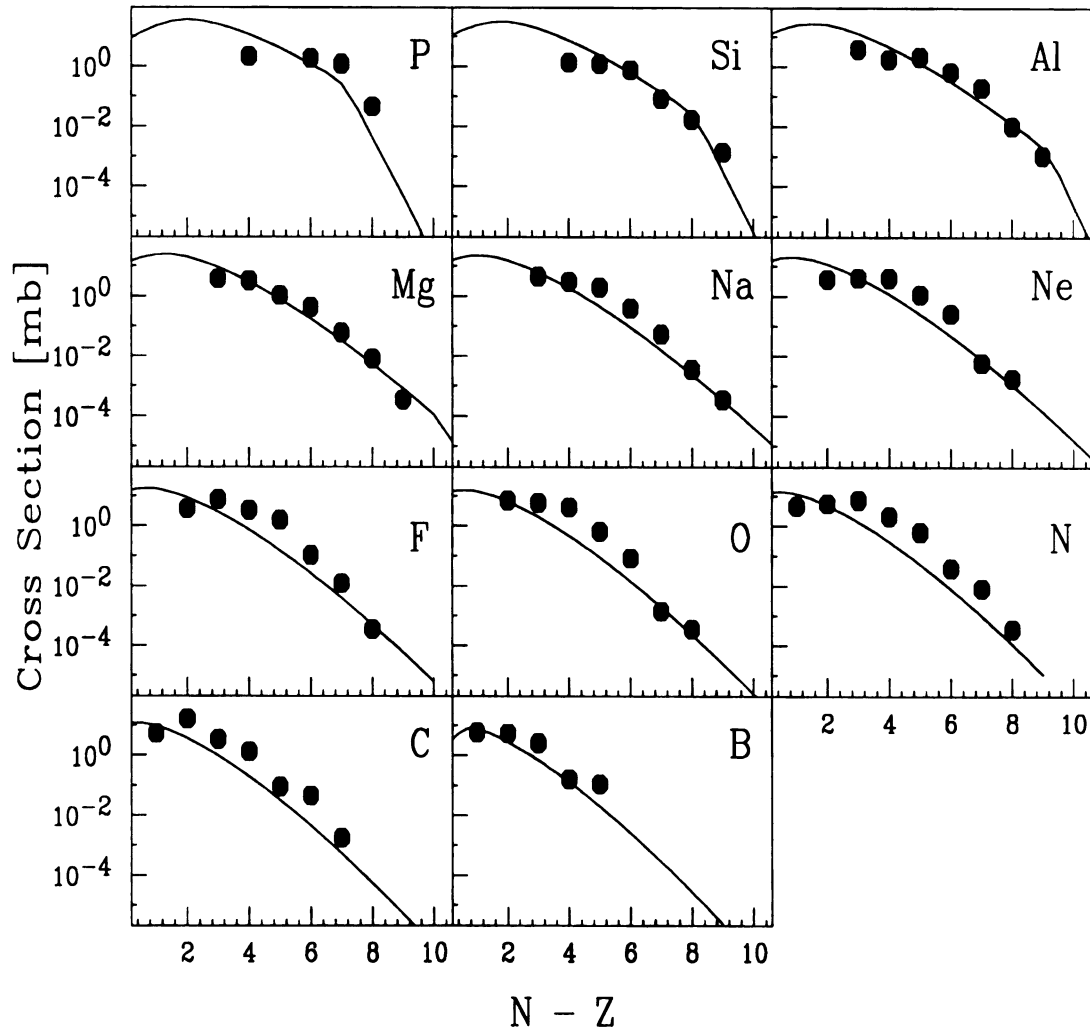
Figure 2.12: Measured reaction cross sections for neutron-rich isotopes (solid points), ranging from ^{38}P to ^{11}B. The full lines indicate the predictions of the semi-empirical formula EPAX [Süm90].
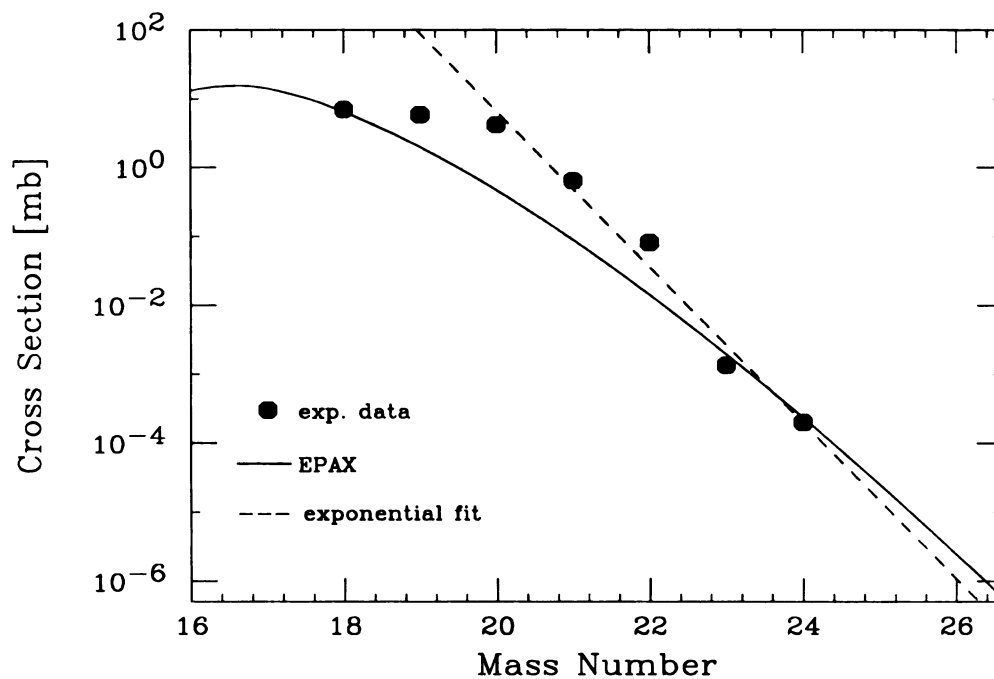
Figure 2.13: Measured reaction cross sections for several oxygen isotopes (solid points), ranging from ^{18}O to ^{24}O. The full line indicates the predictions of the semi-empirical formula EPAX [Süm90], and the dashed line is an exponential fit to the experimental data. The extrapolated production cross sections for ^{26}O agree within a factor of two.

^{26}O. Using this yield of ^{24}O and the two cross section extrapolations (see previous section) of the yields of the lighter oxygen isotopes, we predict that approximately 400 or 800 events of ^{26}O should have been observed. The present data corresponds to an upper limit on the production cross section for ^{26}O of 7 pb at a 90% confidence level. The expected momentum distribution for ^{26}O from the EPAX extrapolation is indicated by the dash dotted line in Figure 2.10b.

As a large effort was put into assuring that the particles of interest were centered at both the intermediate and final focus of the A1200, this result indicates that the lifetime of ^{26}O must indeed be appreciably shorter than the central flight time through the separator (approximately 188 ns). We interpret this to mean that ^{26}O is not particle stable, and that ^{24}O is, in fact, the heaviest bound oxygen isotope.

Finally, there is the issue of the doubly magic nucleus ^{28}O. Only the global prediction of Möller and Nix [Möl88] predict this nucleus to be bound. In a recent experiment at RIKEN Motobayishi *et al.* [Mot95] found a sizeable deformation for the nucleus ^{32}Mg, which indicates the vanishing of the N = 20 neutron shell for exotic nuclei. A search for ^{28}O, which was not possible during the present experiment, was recently performed at GANIL [Tar96], and the experimenters concluded that it is particle unstable.

Chapter 3

Coulomb Excitation of the One-Neutron Halo Nucleus ^{11}Be

3.1   Motivation and Introduction

Coulomb excitation is a well known and powerful tool to study nuclear structure effects. If the charge distributions of the two colliding nuclei do not overlap during the collision process, the measured Coulomb excitation cross sections are directly linked to the electromagnetic matrix elements that characterize the electromagnetic excitation of specific nuclear states. Therefore, Coulomb excitation can provide information on the electromagnetic transition strength, and hence on the nuclear collectivity and deformation. In the past, Coulomb excitation has been used to study low-lying nuclear states by bombarding targets with heavy ions at bombarding energies below the Coulomb barrier. This technique insures that pure Coulomb excitation is the only possible process to excite the nuclei. Until recently only stable nuclei were accessible by this technique.

Recent advances in accelerator technology, together with advances of fragment separation devices allow the production of intense beams of radioactive nuclei. Therefore, it is now possible to use Coulomb excitation to study nuclei far from stability. As mentioned earlier, two different techniques are frequently used to produce the radioac-

tive fragments. The ISOL technique with subsequent acceleration of the secondary beams to energies below the Coulomb barrier allows techniques similar to those used for stable beams. One disadvantage of this technique is that only nuclei with a rather long half-lives are accessible due to the time it takes to separate and (re-)accelerate the fragments.

Projectile fragmentation on the other hand enables one to perform experiments with radioactive nuclei that have a much shorter half-life. The limiting factor here is the flight-time from the production target to the experimental area (typically on the order of a few hundred nano-seconds). However, there are two disadvantages to this approach. The first is that the γ-rays of interest are emitted from a source moving at a sizeable fraction of the speed of light. Therefore, one has to be able to correct for the Doppler-shift and keep the Doppler-broadening of the observed γ-rays small. A more detailed discussion of the consequences these facts have on the photon detection devices can be found in section 3.2.2. The second disadvantage is that it is more difficult to assure 'pure' Coulomb excitation, as nuclear excitation channels are now open as well. However, Coulomb excitation can be assured by requiring extreme forward scattering angles, and by excluding reactions that lead to fragmentation of the incoming radioactive beam. Therefore it is necessary to identify isotopically the fragments before and after the interaction with the secondary – or Coulomb excitation target. One advantage of this method is the possibility of using thick secondary targets to Coulomb excite the projectile. Another advantage is that projectile Coulomb excitation on stable high-Z targets is favored by a factor of Z_T^2/Z_P^2. Figure 3.1 shows a schematic view of the Coulomb excitation process.

A semi-classical description of the Coulomb excitation process that is valid for relativistic energies can be found in [Win79]. In Appendix B a brief recap of the most important points of the theory developed by Winther and Alder will be recapped. The
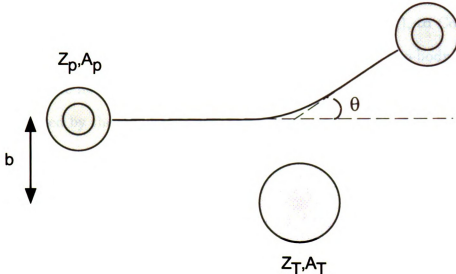
Figure 3.1: Schematic view of the Coulomb excitation process. The minimum impact parameter b is larger than the sum of the radii of the two colliding nuclei.

basic idea one has to keep in mind is that for pure Coulomb excitation the measured Coulomb cross section (σ_{coul}) is proportional to the reduced transition strength $B(\pi\lambda)$, where λ stands for the multipolarity and π is a placeholder to denote either the electric ($\pi \to E$) or magnetic ($\pi \to M$) character of the transition. For the present work we are interested in an E1 transition, and here the Coulomb cross section and the reduced transition strength are related as follows :

$$\sigma_{coul} = \left(\frac{Z_T e^2}{\hbar c}\right)^2 \frac{B(E1)}{e^2} \frac{16\pi}{9} [g_1(\zeta) + (1 - \beta^2) g_0(\zeta)] \qquad (3.1)$$

where ζ is the so-called adiabaticity parameter and the functions $g_{1,0}$ can be evaluated in terms of the modified Bessel functions (see Appendix B and Ref. [Win79] for details).

We employed the technique of intermediate energy projectile Coulomb excitation,

which has previously been shown to be a useful method to study nuclear structure effects in nuclei far from stability (see e.g. [Mot95, Sch96]), to Coulomb excite the one-neutron halo nucleus ^{11}Be. One can describe ^{11}Be as a two-body system consisting of a valence neutron coupled to quadrupole deformed ^{10}Be core. The ground state is dominated by the single particle $1s_{1/2}$ intruder state and not – as would be expected from the simplest shell model – by the $0p_{3/2}$ state. ^{11}Be is the only known halo nucleus with a bound excited state, in fact only the $\frac{1}{2}^+$ ground state and the $\frac{1}{2}^-$ excited state are bound. Both are neutron halo states with root-mean-square radii of approximately 7 fm [Esb94]. Figure 3.2 shows the wave functions of the ground and excited state, as calculated with a Woods-Saxon potential.

Millener *et al.* [1], were the first to realize the special character of this system. They measured the lifetime of the excited state with a Doppler shift technique and found it to be 166(15) fs corresponding to a B(E1) of 0.116(12) e^2fm^2. This is the fastest known E1 transition between bound states in nuclei. There is the possibility that more subtle effects will appear when the lifetime is compared with cross sections for inelastic nuclear scattering because (a) the Coulomb transition amplitude approaches unity at small impact parameters so that first-order perturbation theory may no longer be valid, and (b) the extended halo wave functions may lead to nuclear excitation well beyond distances normally considered 'safe' in Coulomb excitation experiments. The first Coulomb excitation experiment [Ann95] in which a 45 MeV/nucleon ^{11}Be beam bombarded a lead target produced an excitation cross section of 191(26) mb, only 40% of the expected value for pure Coulomb excitation at this energy. This reduction is much larger than what could be reasonably expected from higher-order effects (calculated to be on the order of 10-20% [Ann95, Typ95, Kid96, Ber95]).

We performed a new experiment in which both heavy and light targets (lead, gold, carbon and beryllium) were used in order to investigate the various contributions to
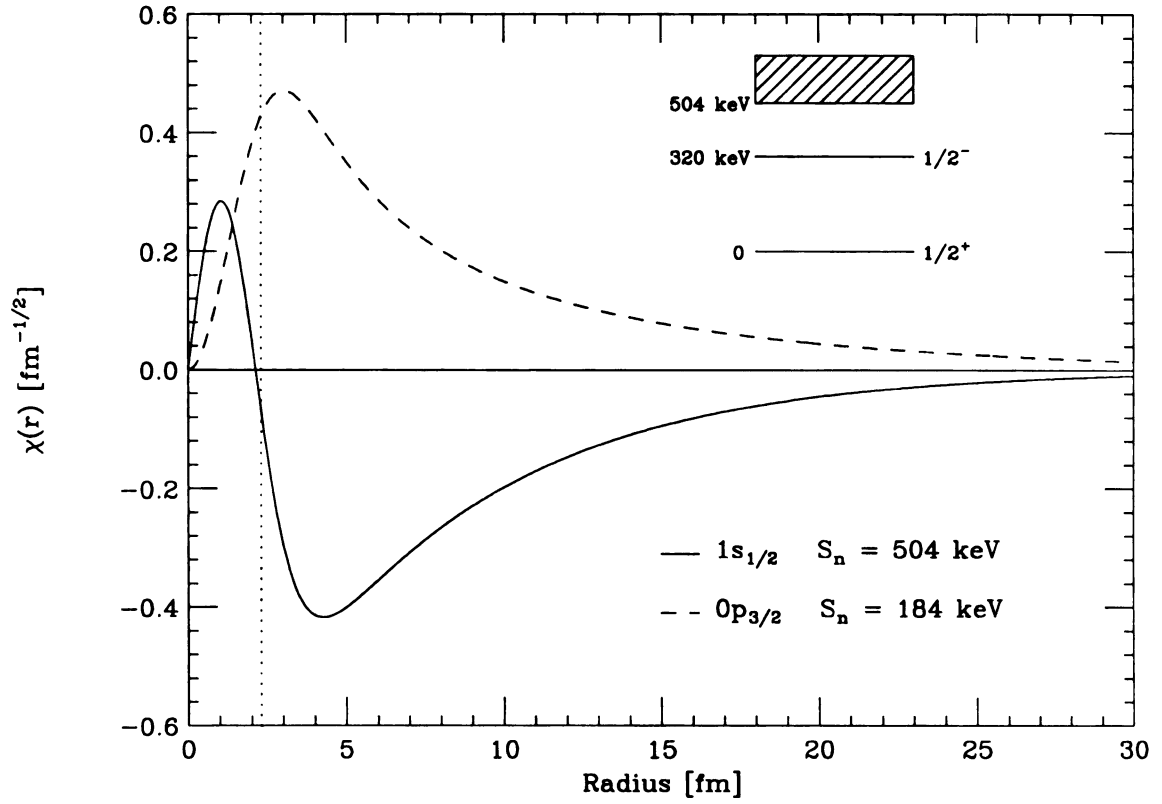
Figure 3.2: The wave function $\chi(r) = rR(r)$ for the two bound states of ^{11}Be, as calculated from a Woods-Saxon potential. The rms radii are 7.3 fm, and 6.3 fm for the $1s_{1/2}$ and $0p_{3/2}$ states respectively. The inset shows the level scheme of ^{11}Be, and the vertical dotted line indicates the rms radius of the ^{10}Be core.

the cross section, which scale differently with Z and A.

3.2 Experimental Apparatus and Analysis

In the following sections the experimental setup used to produce the secondary ^{11}Be beam will be briefly described, and the experimental setup for the actual secondary beam experiment, especially the position sensitive γ-array, will be discussed in some more detail. Thereafter, the analysis process will be discussed, and we will briefly mention how the position-, energy-, and efficiency calibrations were performed. As we are interested in measuring a γ-ray with a relative low energy, we have to take the absorption of the photon inside the target material into account. In section 3.2.6 the implementation of this in the analysis will be described.

3.2.1 Detector Setup

A 80 MeV/nucleon ^{18}O beam from the K1200 cyclotron was used to produce the secondary ^{11}Be beam. The primary ^{18}O beam impinged on a 884 $\frac{mg}{cm^2}$ ^{9}Be target located at the mid-acceptance target position of the A1200 fragment separator [She91]. The magnetic rigidity of the first half of the A1200 was set to a value of Bρ = 3.2439Tm to transport fragments with a mass to charge ratio of 2.75. The energy spread of the fragments was limited to $\pm$ 1% by using the so-called momentum slits located at the first dispersive image of the separator. To further separate ^{11}Be from other fragmentation products, an achromatic wedge (^{27}Al, 425$\frac{mg}{cm^2}$) was placed at the second dispersive image of the A1200. The fragments were identified in the A1200 focal plane using a detector setup consisting of two x-y position sensitive parallel-plate avalanche counters (PPAC) [Swa94], a 500 μm thick PIN diode to record the energy-loss, and a thick plastic stopping detector for the total energy measurement. The time-of-flight was determined with a TAC that measured the time difference between the thick

stopping plastic detector and the cyclotron RF signal. To center the ^{11}Be fragments at the focal plane, the magnetic rigidity of the second half of the separator was set to a value of $B\rho = 3.1166$Tm. Three different fragment species were observed at the focal plane of the A1200, namely ^{9}Li, ^{11}Be, and ^{13}B. The relative intensities of these fragment groups were 1%, 20% and 79% respectively. The three groups were well separated spatially, and in principle one could produce a very pure ^{11}Be secondary beam using the moveable slits located at the exit of the A1200 fragment separator. However, as the counting rate was not a limiting factor, the mixed beam was used for the secondary beam experiment, and individual isotopes were selected on an event-by-event basis during the off-line analysis. The average energy of the ^{11}Be particles was 60.1 MeV/nucleon, and the counting rate at the focal plane was about 40,000 particles per second. The secondary beam experiment took place in the N3 vault and the transmission from the A1200 focal plane to this experimental area was about 50%. The time-of-flight of each particle was measured on an event-by-event basis over the approximately 30 m long flight path, between a thin fast plastic scintillator (0.01" = 0.254 mm, BC404) located after the exit of the A1200 and the zero-degree detector (fast-slow phoswich plastic). A schematic layout of the NSCL facility is shown in Figure 3.3.

The experimental setup for the secondary beam experiment is shown in Figure 3.4. After passing through two x-y position sensitive PPAC detectors [Swa94], the beam impinged on the secondary target. The scattered ions then passed through a third x-y position sensitive PPAC before they were stopped in the zero-degree detector. The position information from the PPACs can in principle be used to track the incoming and scattered particles. However, one of the PPACs was damaged in a previous experiment, and could not be replaced in time for this experiment. Therefore, the PPACs were only used to monitor the relative beam position, and to assure that
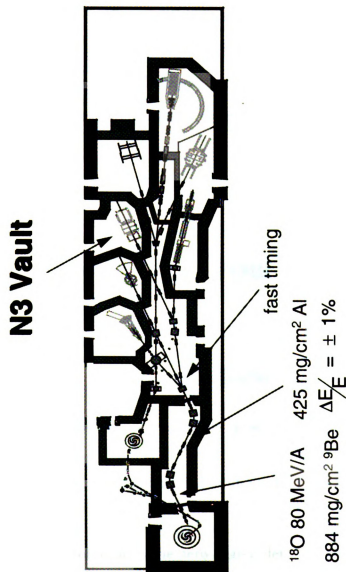
Figure 3.3: Schematic layout of the NSCL facility.

the beam position did not shift over time. The zero-degree detector consisted of a cylindrical fast-slow plastic phoswich detector with a diameter of 10 cm. It was made out of a 0.6 mm thick layer of BC400 (fast), and a 10 cm thick piece of BC444 (slow). This detector defined a half-cone opening angle of approximately $\theta_{max} < 4.1°$. The secondary target was surrounded by the NSCL γ-array which will be described in more detail in the following section. In this series of measurements four different secondary targets (^{208}Pb (80 $\frac{mg}{cm^2}$), ^{197}Au (533 $\frac{mg}{cm^2}$), ^{nat}C (411 $\frac{mg}{cm^2}$), ^{9}Be (195 $\frac{mg}{cm^2}$)) were used to excite the projectiles. All targets had a dimension of 5 cm x 5 cm and are therefore much larger than the secondary beam spot, which has a dimension of approximately 1 cm x 1 cm.
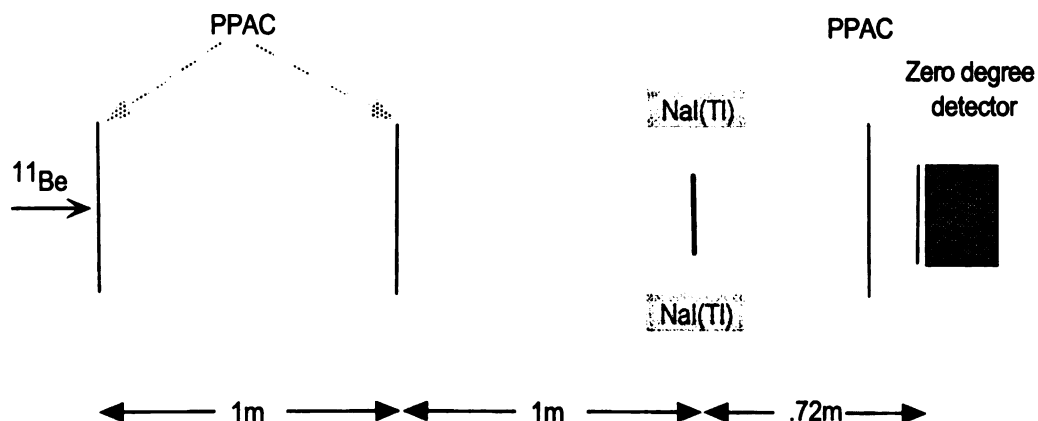
Figure 3.4: Schematic view of the experimental setup used for the projectile Coulomb excitation experiment.

The energy and time resolution in the zero-degree detector used for the isotope identification is shown in Figure 3.5. Here we display the energy loss in the zero-degree detector (from the fast plastic) against the time-of-flight. The left hand side of Figure 3.5 was obtained without the wedge at image #2, while the right hand side of Figure 3.5 shows the result with the wedge and the the 533 $\frac{mg}{cm^2}$ secondary gold

target in place.

One can see the A/Z = 3 line in Figure 3.5a), and the reduction of the number in fragments that reach the zero degree detector after inserting the wedge at image #2, in Figure 3.5b).

3.2.2 The NSCL γ-array

To measure the deexcitation γ-rays following intermediate energy projectile Coulomb excitation, a high efficiency photon spectrometer is needed. As the spectrometer is to be used with a wide variety of radioactive beams, it has to fulfill certain requirements. Due to the sometimes low beam intensities of the radioactive beams, a large angular coverage and high efficiency over a broad range of γ-ray energies are necessary. Since the photons are emitted from a moving source – typically $\beta \approx 0.3$ – one also has to be able to correct for the Doppler-shift of the detected γ-rays, and try to minimize the Doppler-broadening of the photopeak. Therefore, a high granularity of the detection system is desirable. These requirements favor a compact array of position sensitive NaI(Tl) detectors over a less compact array of non-position sensitive high purity germanium (HPGe) detectors. Although HPGe detectors have a far superior intrinsic energy resolution than NaI(Tl) detectors, their intrinsic photopeak efficiency is lower. In addition, the intrinsic energy resolution of the NaI(Tl) detectors is comparable to the limit in energy resolution set by the Doppler-broadening and is therefore sufficient for our purposes. The NSCL γ-array [Gla97] consists of 38 position sensitive NaI(Tl) detectors arranged in three concentric rings parallel to the beamline. The detectors are on loan from a decommisioned PET machine at Washington University in St. Louis. Each NaI(Tl) crystal is 18 cm long, has a diameter of 5.75 cm, and is enclosed in a 0.45 mm thick aluminum shield. The crystals are connected to a photomultiplier tube on each end, and the position and energy of the incident photons can be recon-
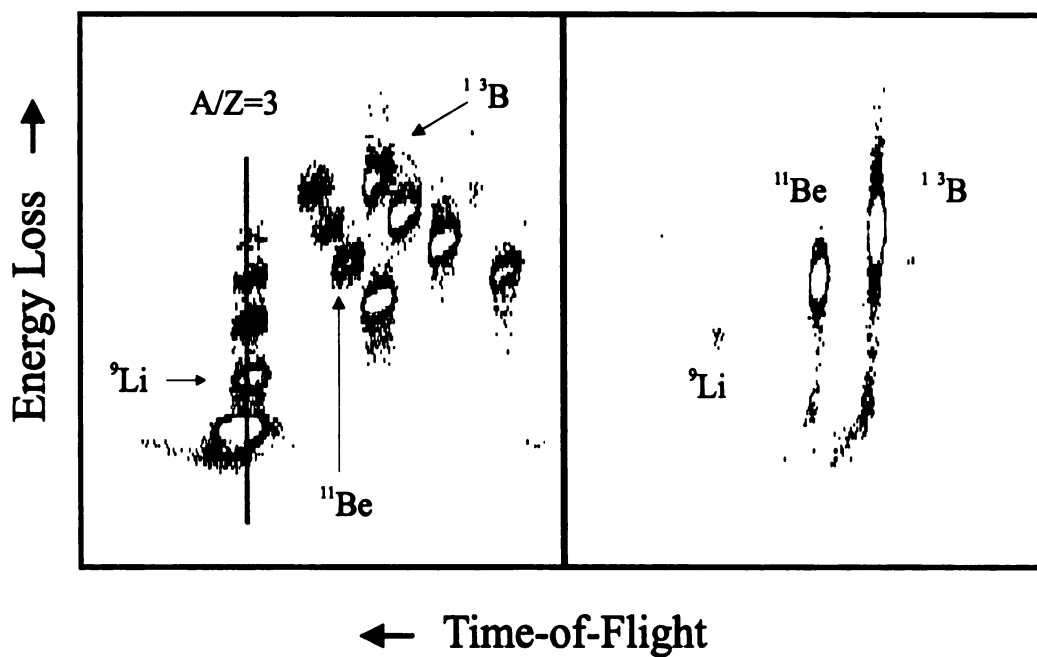
Figure 3.5: Energy loss vs. time-of flight (in arbitrary units), as recorded in the zero degree detector and the beamline timing detector. The left panel was recorded without the wedge at image #2. The right panel was recorded with the wedge and the 533 $\frac{mg}{cm^2}$ secondary gold target.

structed from the two photomultiplier tube signals. Assuming a coordinate system with its origin in the center of the crystal and its x-axis along the crystal axis, the light yield of the two photomultipliers ($Y_{1,2}$) is proportional to :

$$Y_{1,2} \propto e^{\pm x} \tag{3.2}$$

The energy and position of the incident photon are then given by :

$$Energy \quad \propto \quad \sqrt{Y_1 * Y_2} \tag{3.3}$$

$$Position \quad \propto \quad log(\frac{Y_1}{Y_2}) \tag{3.4}$$

To shield against background γ-rays, the whole array is surrounded by a 16.5 cm thick layer – this corresponds to about 6 tons – of low background lead. A schematic side and front view of the mechanical setup is shown in Figure 3.7.

A photograph of the support structure and the detector system is shown in Figure 3.6

The photograph in Figure 3.8 shows the actual NSCL γ-array with part of the lead shielding in place.

3.2.3 Position Calibration

In the following the procedure used for the position calibration for each of the 38 NaI(Tl) detectors will be described. As mentioned earlier, it is very important to achieve good position resolution as well as an accurate position determination, as we have to correct for the Doppler-shift of the photons of interest. As described in section 3.2.2, each NaI(Tl) crystal is read out by two photomultipliers. The position of the incident photon is, according to equation 3.4, proportional to the logarithm of
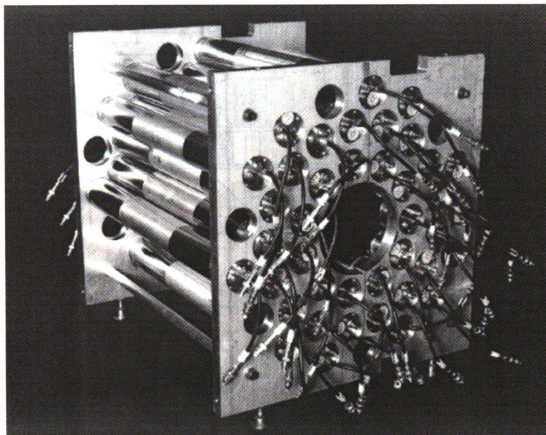
Figure 3.6: The NSCL γ-array.
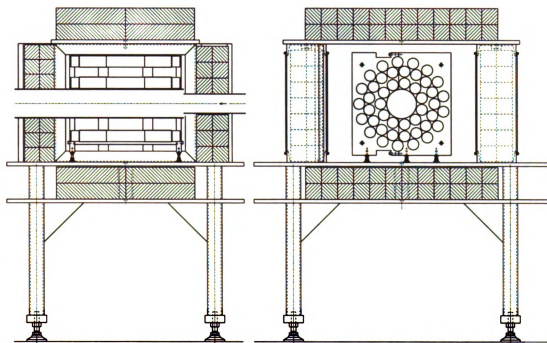
Figure 3.7: Schematic view of the mechanical setup of the NSCL γ-array. The support structure and the lead shielding (hatched areas) can be seen. The target is located in the center of the beampipe. The beam enters from the left in the right hand picture, and the Figure on the left hand side shows the array in the beam direction.
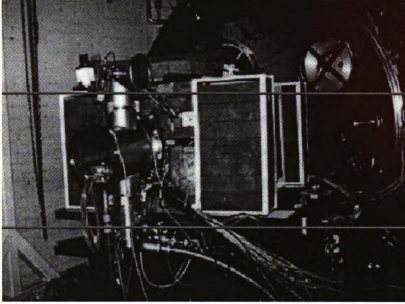
Figure 3.8: The NSCL γ-array, with part of the low background lead shielding in place.

the ratio of the two light. The pseudo parameter POSITION was recorded for each detector, and the following formula was used to calculate it :

$$POSITION = 2000 + 1000 * log\left(\frac{Y_1}{Y_2}\right) \qquad (3.5)$$

This gives the position in channel numbers, and places a photon that hits the center of the detector into channel 2000 as described below. To calibrate the absolute position we used a well collimated ^{60}Co source. This source emits two γ-rays with energies of 1173.2 keV and 1332.5 keV, respectively. The calibration was performed in a very labor intensive way, as each detector had to be calibrated individually. For the calibration, a single detector was placed inside a cavity made out of low background lead bricks, to shield the detector against background radiation and to collimate the ^{60}Co source. The γ-rays from the source reached the detector through a small hole and illuminated about 1 cm of it. Each detector had a length scale (tape measure)

attached to the outside, which ranges from 0 cm to 20 cm, and is used as a reference mark.

In the initial step the detector was placed inside the cavity, so that the center of each crystal (position 10 cm) was illuminated by the ^{60}Co source. We made sure that the actual signal height from each phototube was approximately equal by matching the amplifier outputs on an oscilloscope. This places the pseudo parameter POSITION around channel number 2000 for the central position (10 cm). Figure 3.2.3 shows the raw ADC output from the two photomultiplier tubes of one crystal – panel a) and b) – as well as the calculated energy, using both photomultipliers (c) – see equation 3.3 – and the calculated position (d) –see equation 3.5– for the case that the source illuminated the center of the detector. It should be pointed out that the energy was not yet calibrated this point and that therefore all values are given in channel numbers.

This measurement was repeated eight more times for each detector in position bins of 2 cm width (2 cm, 4 cm, ..., 18 cm), and the centroids of the calculated positions were recorded. The actual position of the detector inside the cavity was determined by removing the source, and peeping through cross hairs in the collimator hole onto the tape measure on the detector. We performed a cubic fit to the data, and the resulting fit coefficients were written into a lookup table to transform the position in channel numbers into a calibrated position in centimeters. A typical example of the achieved position calibration – given as position in centimeters versus calculated position in channel numbers – for one detector is shown in Figure 3.10, together with the results from the cubic fit. The vertical error bars shown represent the actual width of the fitted position distribution (see Figure 3.2.3d). One has to be sure that the cubic fit to the data does not turn over within the range of the detector. This would result in an ambiguity of the determined position.
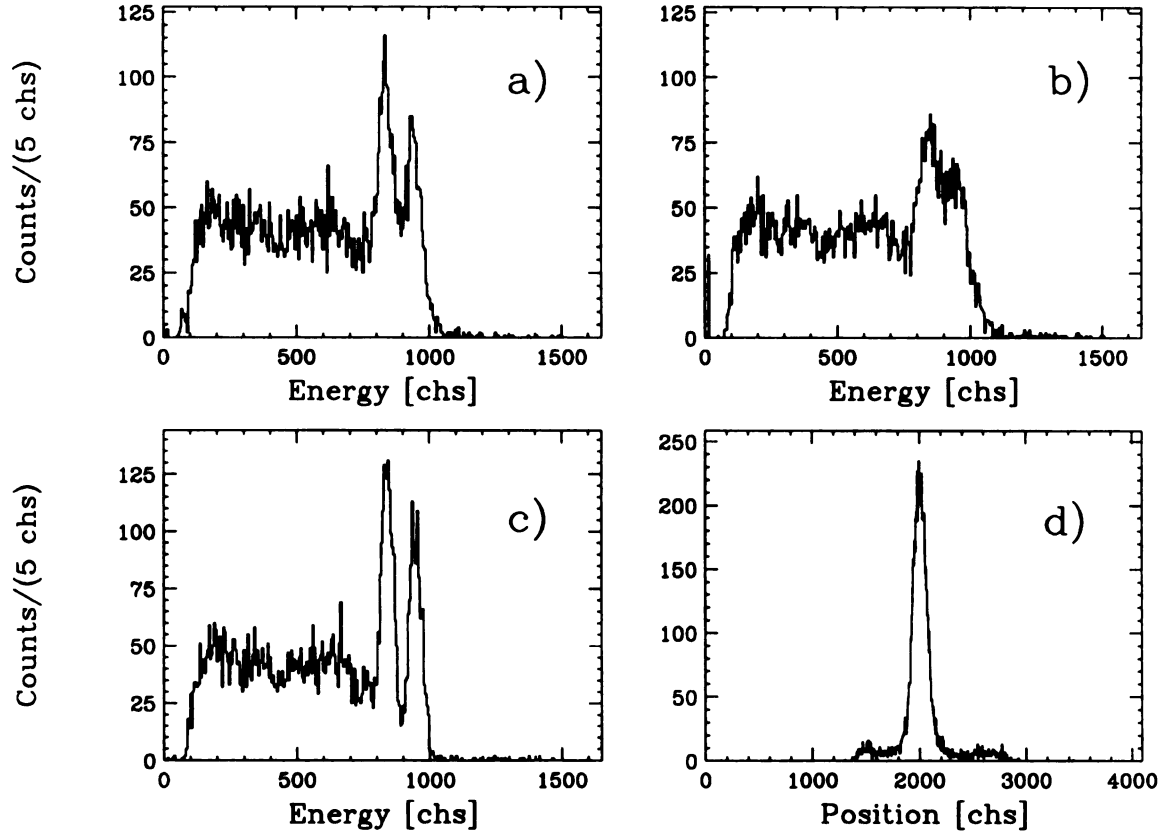
Figure 3.9: The raw ADC output from the two phototubes of a typical detector (a, b), as well as the derived energy from combining the two raw signals (c) and the calculated position (d), for a ^{60}Co source in the center of the detector.
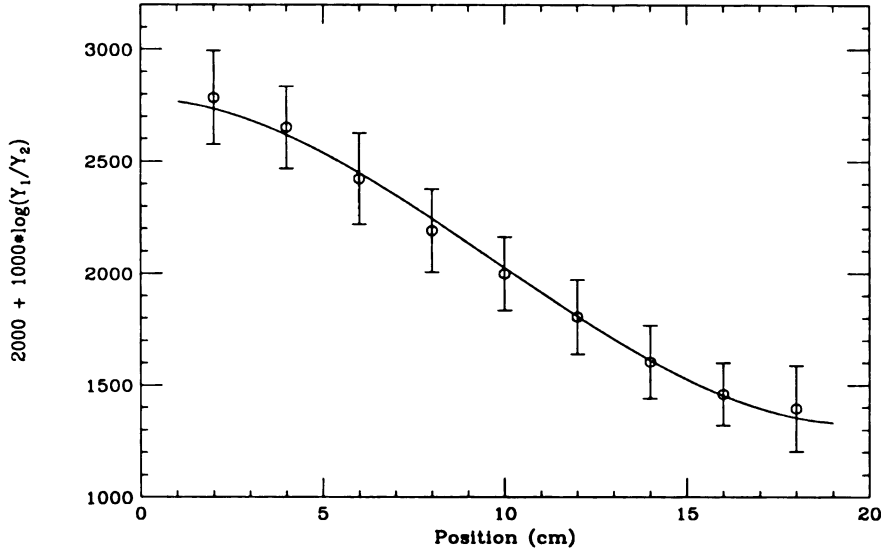
Figure 3.10: Typical position calibration spectrum for one detector. Shown is the actual detector position (in cm) versus the calculated position from the two photomultiplier signals (in channel number). The points represent the actual measurements, the error bars represent the width of the distribution, and the solid line shows a cubic fit to the data.

The best position resolution is of course achieved when a very strong correlation between the calculated position and the actual position exists. The average position resolution achieved was better than 2 cm. This corresponds to an angular resolution of better than 10° in the present configuration. After the detectors were placed in the array support structure and surrounded by the approximately 6 tons of low background lead, the validity of the position calibration was checked again. This time we placed a source at the secondary target position in the center of the array and recorded the correlation between the observed energy and the calibrated position. We expect to see no correlation between the energy and calibrated position, in this case of isotropic emission at rest in the laboratory system, and this is demonstrated nicely in Figure 3.12 for the [228]Th source.

3.2.4 Energy Calibration

All 38 detectors that form the NSCL γ-array need also to be energy calibrated. This task was performed after the detectors were placed in the support structure and the low background lead shielding was in place. We placed different γ-ray sources in the center of the array, in the same position that was used for the secondary targets during the experiment. To cover a wide range of photon energies we used three different sources, namely ^{88}Y, ^{152}Eu, and ^{228}Th. As one can see in equation 3.3, the deposited energy in each crystal is proportional to the square root of the product of the light yield from the two photomultipliers. We require a position dependent energy calibration and therefore divide each detector into ten slices of equal size. This was done using the pseudo parameter POSITION (see equation 3.5), and not with the calibrated position pseudo parameter, as we did not want to introduce additional sources of error. For each position slice we used a linear fit to calibrate the energy. The nice linear dependence between the calibrated energy (in keV) and the raw energy (in channels) calculated via equation 3.3 can be seen for one specific position slice in Figure 3.11. In this plot, we show the calibration points from the ^{88}Y (898.1 keV, 1836.1 keV) and the ^{228}Th (235.6 keV, 2651 keV) source. To check that there is no correlation between the calibrated position and the calibrated energy, we plot one against the other in Figure 3.12 for one individual detector, using the ^{228}Th source.

In Table 3.1 we demonstrate the effectiveness of the energy calibration for four calibration γ-rays spanning an energy range from 235.6 keV to 2615 keV, for the eleven detectors that form the inner ring of the NSCL γ-array. We also present the energy resolution achieved for those γ-rays. Typically we obtained a resolution of better than 15% for the 235.6 keV photon, better than 9% for the 898.1 keV photon, better than 7% for the 1836.1 keV photon, and near 6% for the 2615 keV photon.
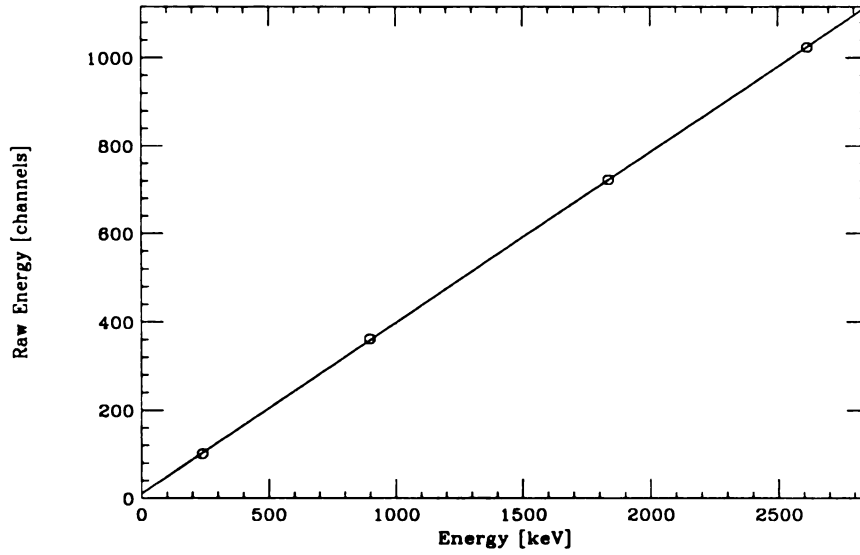
Figure 3.11: Typical energy calibration spectrum for one detector and position slice, using the ^{88}Y and ^{228}Th calibration sources. The open circles represent the measured data points, whereas the solid line represents a linear fit to the data.

However, one can see in Table 3.1, that some of the detectors had rather poor energy resolution and were therefore excluded from the subsequent data analysis. This point will be discussed in the next section on the efficiency calibration, as well as in section 3.3.

During the experiment we performed several so-called 'fast calibrations', using a ^{152}Eu source, to check for a possible drift in the energy calibration. For the 'fast calibrations', we did not put the source at the secondary target position – which would have required venting part of the beamline – but placed the source between the support structure and the low background lead shielding. Even though the detectors did not get illuminated equally under this condition, the energy signals were sufficient to provide us with a few data points to check the stability of the energy calibration. The detectors turned out to be stable in time, so that no additional changes to the original energy calibration were needed.
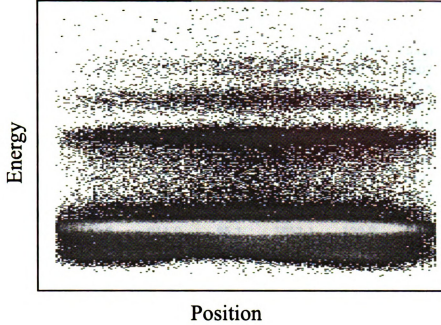
Figure 3.12: Calibrated position versus calibrated energy for one individual detector using the ^{228}Th source.

3.2.5 Efficiency Calibration

The efficiency calibration of the NaI(Tl) detectors was performed with a set of calibrated sources. As with the energy calibration we wanted to cover a wide range of photon energies. Therefore, we used a calibrated ^{152}Eu source, as well as a calibrated ^{88}Y, and a calibrated ^{228}Th source which emit γ-rays with known intensities in the energy range between 244.7 keV and 2615 keV. The sources where placed in the middle of the array in the same position that was occupied by the secondary target during the experiment. The energy spectra from each detector were again divided into ten position bins of equal width. The efficiency for each bin was determined by counting the number of γ-rays registered in each position bin – corrected for the live-time of the data acquisition system – and comparing them to the expected number from the calibrated sources. The result for one specific detector is displayed in Figure 3.13.

Table 3.1: Energy calibration and energy resolution for the eleven detectors that form the inner ring of the NSCL γ-array, using the ^{88}Y and ^{228}Th calibration sources.

Detector	$E_\gamma = 235.6$ keV channel	FWHM	$E_\gamma = 898.1$ keV channel	FWHM	$E_\gamma = 1836.1$ keV channel	FWHM	$E_\gamma = 2615$ keV channel	FWHM
01	232.2	33.6	904.8	81.6	1838.9	120.1	2602.0	153.1
02	232.8	34.2	915.0	84.6	1855.1	120.5	2618.4	166.3
03	232.1	33.4	907.4	81.3	1843.2	108.4	2602.2	133.5
04	231.4	38.6	911.3	103.0	1852.8	131.5	2619.2	179.1
05	229.6	31.6	907.2	82.6	1843.1	107.5	2607.3	125.0
06	229.8	30.2	904.3	76.7	1839.5	96.5	2602.1	122.5
07	230.0	32.6	902.0	81.7	1834.6	107.0	2602.2	134.3
08	230.6	30.1	906.1	77.4	1841.3	96.9	2605.0	133.5
09	230.0	40.1	900.7	103.7	1836.2	127.7	2601.9	180.1
10	230.6	35.8	911.0	95.1	1853.1	122.9	2614.0	165.2
11	227.7	32.9	894.0	81.9	1820.6	107.7	2577.0	138.0

The solid lines connect the results for specific position bins, and are only drawn to guide the eye. The energies displayed in this Figure are (from top to bottom) : 244.7 keV, 344.3 keV, 778.9 keV, 964 keV, 1100 keV, and 1408 keV.

The accuracy of the efficiencies determined by this method was checked by a different method to measure the efficiencies. The ^{88}Y source emits two correlated photons, and by measuring the coincidence rate, one can deduce the efficiencies at those energies (898 keV and 1836 keV). The obtained result agreed well with the result obtained by using the above mentioned method.

To represent the steep drop in the efficiency with increasing photon energy, we fit the calculated efficiencies with a function of the form :

$$\epsilon = e^{-(a_0 + a_1 * log(E/(50keV)))} * e^{\left(\frac{f}{log(E/(50keV))}\right)} \tag{3.6}$$

The fit parameters a_0, a_1, and f were written into a table. The second term in equation 3.6 models the drop in the efficiency for the low energies. In Figure 3.14 the results from the efficiency calibration (data points) are displayed together with the results
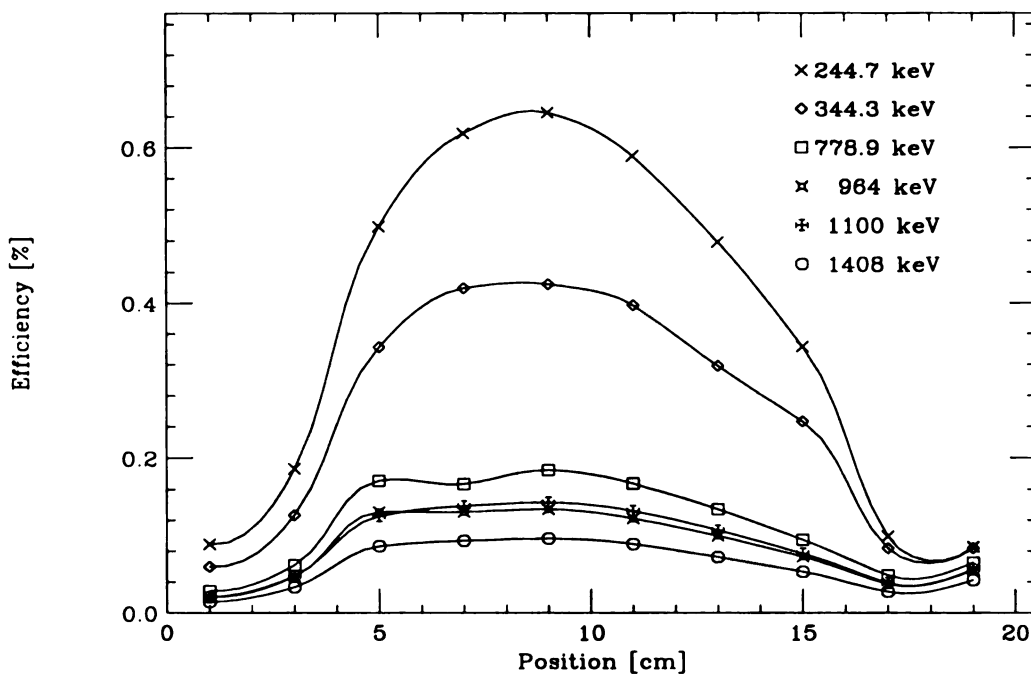
Figure 3.13: Efficiency for a typical NaI(Tl) detector of the NSCl γ-array, as a function of detector position for several different photon energies from the calibration sources. The lines represent the results for different energies, and are only drawn to guide the eye.

obtained from the fit using the above formula (solid lines). The results are shown for each of the ten position slices from one specific detector. As one can clearly see in this double-logarithmic plot, we can achieve a very good efficiency calibration over the whole range of calibration energies for the inner six position slices. However, for the outer two – on each end of the crystal – the energy dependence of the efficiency cannot be reproduced accurately by equation 3.6. Different fit functions were tested as well, but did not lead to a better overall agreement to the measured efficiencies. The extremely steep drop in the measured efficiency for the low photon energies in the outer position bins, can of course also be seen in Figure 3.13. The steep drop is caused by two different factors : a) absorption of the low energy γ-rays in the beampipe, and b) the absorption inside the crystal itself. The latter attenuates the signal from a

low energy photon produced close to one phototube too much to permit a trigger of the discriminator connected to the other phototube. Our main focus is on the 320 keV γ-ray from the $\frac{1}{2}^+ \rightarrow \frac{1}{2}^-$ transition in ^{11}Be. Therefore, it is very important to determine the detection efficiency for the low photon energies very accurately. Due to the very good statistics in the photopeak from the transition of interest (see Figure 3.20), we were able to choose only those detectors for which a very good efficiency calibration over the whole energy range of the calibration sources could be achieved. This way, we were able to minimize the error introduced by the efficiency calibration in our cross section calculation. Only three inner ring detectors were used for the rest of the analysis, and even for those detectors, the two outermost position slices on each side were omitted. As mentioned above, this could be done because we had enough statistics in the photopeak of interest.

Our restriction of only using the six inner position slices of each detector reduces the angular coverage (in theta) of the NSCL γ-array from approximately 45° to 135° for all ten slices to about 60° to 120°. As we are interested in γ-rays emitted from a source moving at about 1/3 of the speed of light ($\beta \approx 0.34$), we have to take the Doppler-shift of the emitted photons into account and calculate the efficiency at the Doppler-shifted energy. The Doppler-shifted energy depends on the emission angle of the photon as follows :

$$E_\gamma = \frac{E_{\gamma 0}\sqrt{1 - \beta^2}}{1 - \beta cos\theta} \tag{3.7}$$

where E_γ stands for the Doppler-shifted energy observed in the laboratory frame, $E_{\gamma 0}$ is the unshifted photon energy in the moving frame (320 keV in our case), β is the velocity of the projectile with respect to the laboratory frame in units of the speed of light, and θ is the γ-ray emission angle in the laboratory relative to the beam axis.
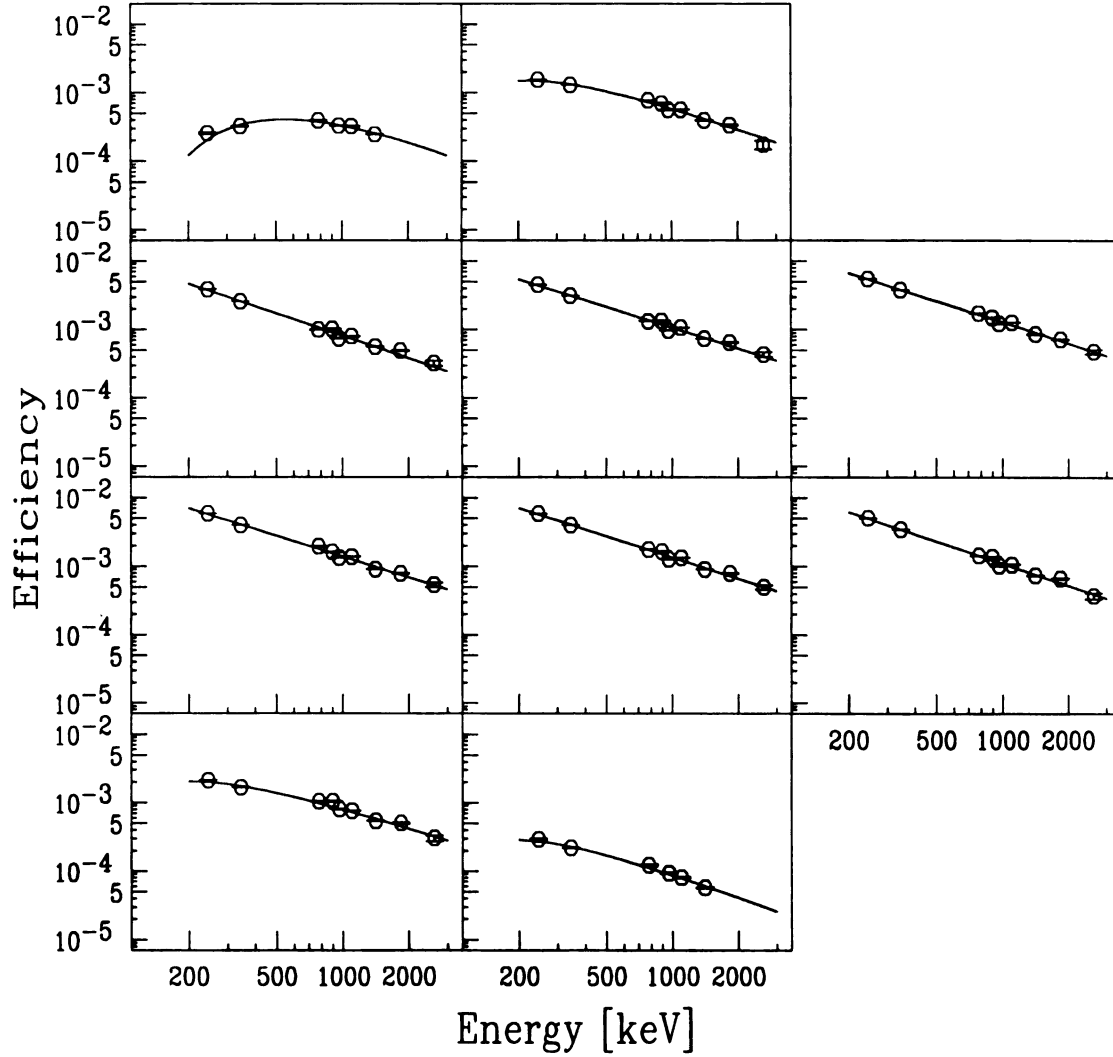
Figure 3.14: Efficiency for a typical NaI(Tl) detector divided into ten position slices. The open points with error bars represent the measured efficiencies, and the full lines show a fit to the data, using equation 3.6. The position slices are in ascending order from left to right, and from top to bottom.

The angular dependence of the Doppler-shifted energies can be seen in Figure 3.15. For the actual NSCL γ-array the Doppler-shifted energy varies between 396 keV and 222 keV. For the limited angular range chosen for the analysis, the energy only varies between 361 keV and 256 keV.
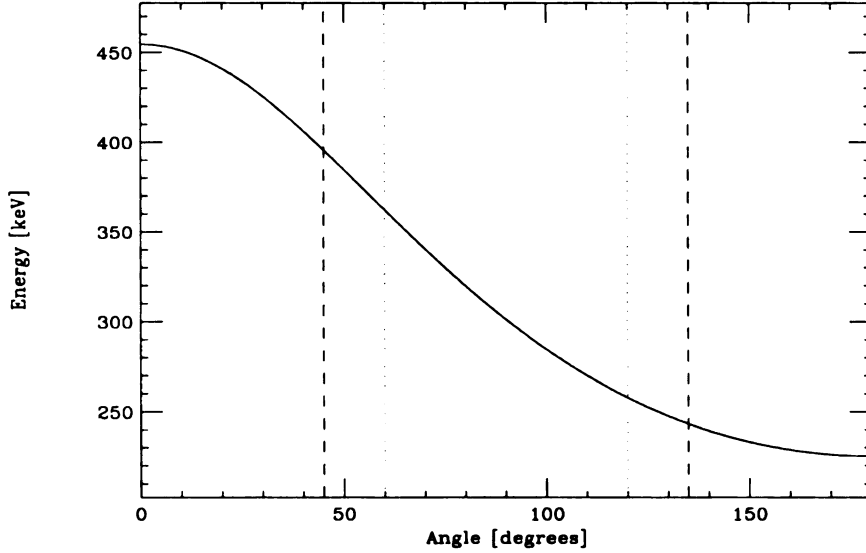
Figure 3.15: Doppler-shifted γ-ray energy in the laboratory frame for the 320 keV photon as a function of emission angle in the laboratory frame. The vertical lines indicate the angular coverage of the NSCL γ-array (- -) and the restricted angular coverage used for the analysis ($\cdots$).

The error introduced by the efficiency calibration in the cross section calculation is smaller than 5% for the $\frac{1}{2}^+ \rightarrow \frac{1}{2}^-$ transition in ^{11}Be.

We were also able to measure the 3368 keV γ-ray from the $2^+ \rightarrow 0^+$ transition from the first excited state to the ground state in ^{10}Be. We populate this excited state in the nuclear breakup of ^{11}Be on the light (C, Be) targets. The observed Doppler-shifted energy for this γ-ray ranges from 3816 keV to 2707 keV. At the NSCL, there is no calibrated γ-ray source available that covers this energy range. Therefore, we had to extrapolate the efficiency from the measured efficiencies at the highest available photon energies. This introduces an additional error. Whereas the efficiency for the 1408 keV and 2615 keV photon is reproduced to better than 9% by our fit, we assume

– in a conservative approach – that this number doubles for the 3368 keV photon.

The detector efficiency was combined with the angular distribution of the emitted photons to determine the detection efficiency for the photons of interest. The angular distribution of the 320 keV γ-ray from the $\frac{1}{2}^- \rightarrow \frac{1}{2}^+$ transition in ^{11}Be is isotropic in the projectile rest frame. For the 3368 keV γ-ray from the $2^+ \rightarrow 0^+$ transition from the first excited state to the ground state in ^{10}Be we have to take the population of the m-substates into account as well. This was done by using the formalism as described in Ref. [Win79] (see also Ref. [Sch97]). A MATHEMATICA [Mat97] code was developed to handle the above calculations.

3.2.6 Absorption of Photons in the Target

The following section describes the absorption of photons in the target material. As the γ-ray from the transition of the first excited state to the ground state in ^{11}Be has only an energy of 320 keV, absorption is an important process, especially since we used several rather thick secondary targets to Coulomb excite the incoming ^{11}Be nuclei. The method used follows closely the description found in Appendix G of the Table of Isotopes [Fir96]. The decrease in intensity of a parallel beam of photons passing through an absorber of thickness t is, according to Wapstra et al. [Wap59], given by :

$$I = I_0 * e^{-\frac{t}{t_{1/2}}} \tag{3.8}$$

where I_0 is the incoming photon intensity, and I stands for the photon intensity after passing through the absorber material. The quantity $t_{1/2}$ is the so called half-thickness, and depends on the target material as well as the photon energy. It can

be expressed as :

$$t_{1/2} = \frac{A}{N_A * \rho * \sigma(E)} \tag{3.9}$$

where A denotes the atomic mass, N_A is Avogadro's number, ρ is the density of the absorbing material, and $\sigma(E)$ is the energy and material dependent atomic cross section. The atomic cross sections are taken from the tables of Storm and Israel [Sto70]. The cross sections take all four interaction processes of photons with matter into account, namely the photoelectric absorption, coherent (Rayleigh) scattering, incoherent (Compton) scattering, and pair production. At low photon energies the most important process is the first, in which the photon is absorbed by an atom, that subsequently emits an electron. The atom is left in an excited state and returns to the ground state via the emission of Auger electrons or x-rays. Also important at low energies is coherent- or Rayleigh scattering. In this process, the photon gets deflected by the atomic electrons without losing energy. In the middle-energy regime, between approximately 0.2 and 5 MeV, the most important process is the incoherent (inelastic) Compton scattering. In this process the photon is scattered from an atomic electron, but this time it transfers momentum and energy to the struck electron, sufficient to put it into an unbound state. At higher energies pair production becomes an important process. This process involves the creation of an electron-positron pair in the field of a massive charged particle. The high energy electron of this pair produces bremsstrahlung radiation as well as ionization along its path while the positron is eventually annihilated with the production of new photons. For photon energies below the rest mass of an e^+e^- pair (1.022 MeV), the latter process cannot take place. We also neglect the coherent Rayleigh scattering, as this is only important for so-called narrow beam experiments, where both the source and the detector are well

collimated, and this is not the case for our experiment.

To gain a qualitative understanding of the size of the absorption effects encountered, we calculate the absorption for a 300 keV photon, emitted from a pointlike source in the middle of the target. The γ-ray then traverses through a different amount of target material, depending on its emission angle, so that the constant thickness t in equation 3.9 has to be replaced by one that is angle dependent, specifically $\frac{t}{2*|cos\theta|}$. The transmission probability for the different targets as a function of photon emission angle is shown in Figure 3.16. The actual NSCL γ-array covers an angular range from approximately 45° to about 135°. It is interesting to note that the 411 $\frac{mg}{cm^2}$ carbon target actually attenuates the photon intensity more than the 80 $\frac{mg}{cm^2}$ lead target.
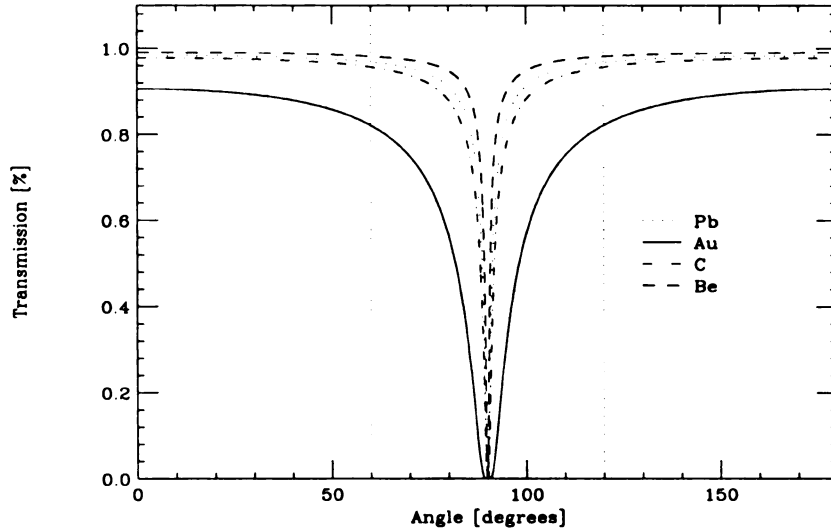
Figure 3.16: Transmission probability for a 300 keV γ-ray through the secondary targets as a function of photon emission angle, for the lead ($\cdots$), gold (—), carbon (- · -) and berylium (- -) targets used in this experiment. The vertical lines indicate the angular coverage used for the analysis.

This first, qualitative attempt, however, needs to be refined, since for the light targets (C, Be), the finite target size (5 cm x 5 cm) is not sufficient to absorb the γ-ray completely, even when it is emitted under 90°. Therefore one has to take the finite

target size into account for the transmission probability calculations. We calculate the transmission probability for photons emitted at 90° to be about 55% (C) and 65% (Be) respectively. We also cannot use a single, fixed energy for the emitted photons, as was done in our first attempt. As we are interested in γ-rays emitted from a source moving at about 1/3 of the speed of light, we have to take the Doppler-shift of the emitted photons into account as well. The Doppler-shifted energy depends on the emission angle of the photon as shown in equation 3.7. For the actual NSCL γ-array the Doppler-shifted energy varies between 396 keV and 222 keV, and for the limited angular range we choose for the analysis, the energy varies between 361 keV and 256 keV. Figure 3.17 depicts the energy dependence of the atomic cross section (including photoelectric absorption, and Compton scattering) as given by Storm and Israel [Sto70] for γ-ray energies between 200 and 500 keV for the four target materials used in the present experiment. The open circles represent the tabulated values, and the error bars represent the possible error of 5% as given in [Sto70]. The smooth lines connecting the points are our fits to the data as used in the following evaluation. To reproduce the very steep drop off of the atomic cross section with the increase in photon energy for the heavy targets (Pb, Au) we used a third order exponential fit of the form :

$$\sigma(E) = y_0 + A_1 e^{-\frac{E_\gamma - x_0}{t_1}} + A_2 e^{-\frac{E_\gamma - x_0}{t_2}} + A_3 e^{-\frac{E_\gamma - x_0}{t_3}} \tag{3.10}$$

where E_γ represents the Doppler-shifted energy of the emitted γ-ray. For the light targets (C, Be), we use a simple quadratic fit, of the form :

$$\sigma(E) = y_0 + A_1 E_\gamma + A_2 E_\gamma^2 \tag{3.11}$$

where E_γ again stands for the Doppler-shifted energy of the emitted γ-ray. The fit

parameters are listed in Table 3.2.

Table 3.2: Parameters used to fit the atomic cross sections.

Target	A_1	A_2	A_3	t_1	t_2	t_3	x_0	y_0
Pb	185.4	89.32	62.01	115.7	10.42	106.9	196.58	37.62
Au	155.3	69.36	44.88	118.7	28.47	117.1	199.24	33.52
C	$-5.02 \cdot 10^{-3}$	$3.75 \cdot 10^{-6}$	3.30					
Be	$-3.47 \cdot 10^{-3}$	$2.75 \cdot 10^{-6}$	2.22					

Putting all the pieces together, we end up with a transmission probability as shown in Figure 3.18. The asymmetry of the Figure is caused by the Doppler-shift.

One can further generalize this result and neglect the assumption that all photons are produced in the center of the target. To eliminate the dependence on the production place, we integrate equation 3.8 over the target thickness :

$$I \;=\; I_0 * \int_0^t e^{-\frac{x}{t_{1/2}*|cos\theta|}} * \frac{1}{t}dx$$

$$=\; -I_0 * \frac{t_{1/2}*|cos\theta|}{t} \int_0^{\frac{t}{t_{1/2}*|cos\theta|}} e^{-x}dx \qquad (3.12)$$

here, t stands for the target thickness (note, that we have to use the full target thickness now, and not only half of it, as before). Solving the integral leads to the following expression for the transmission probability :

$$I = I_0 * \frac{t_{1/2}*|cos\theta|}{t}\left(1 - e^{-\frac{t}{t_{1/2}*|cos\theta|}}\right) \qquad (3.13)$$

We can easily compare this result to the previous one, when we look at a series expansion of the two. Substituting $s = \frac{t}{t_{1/2}*|cos\theta|}$ one can expand equation 3.13 into :

$$I = I_0 \left(1 - \frac{s}{2} + \frac{s^2}{6} - \frac{s^3}{24}\cdots\right) \qquad (3.14)$$
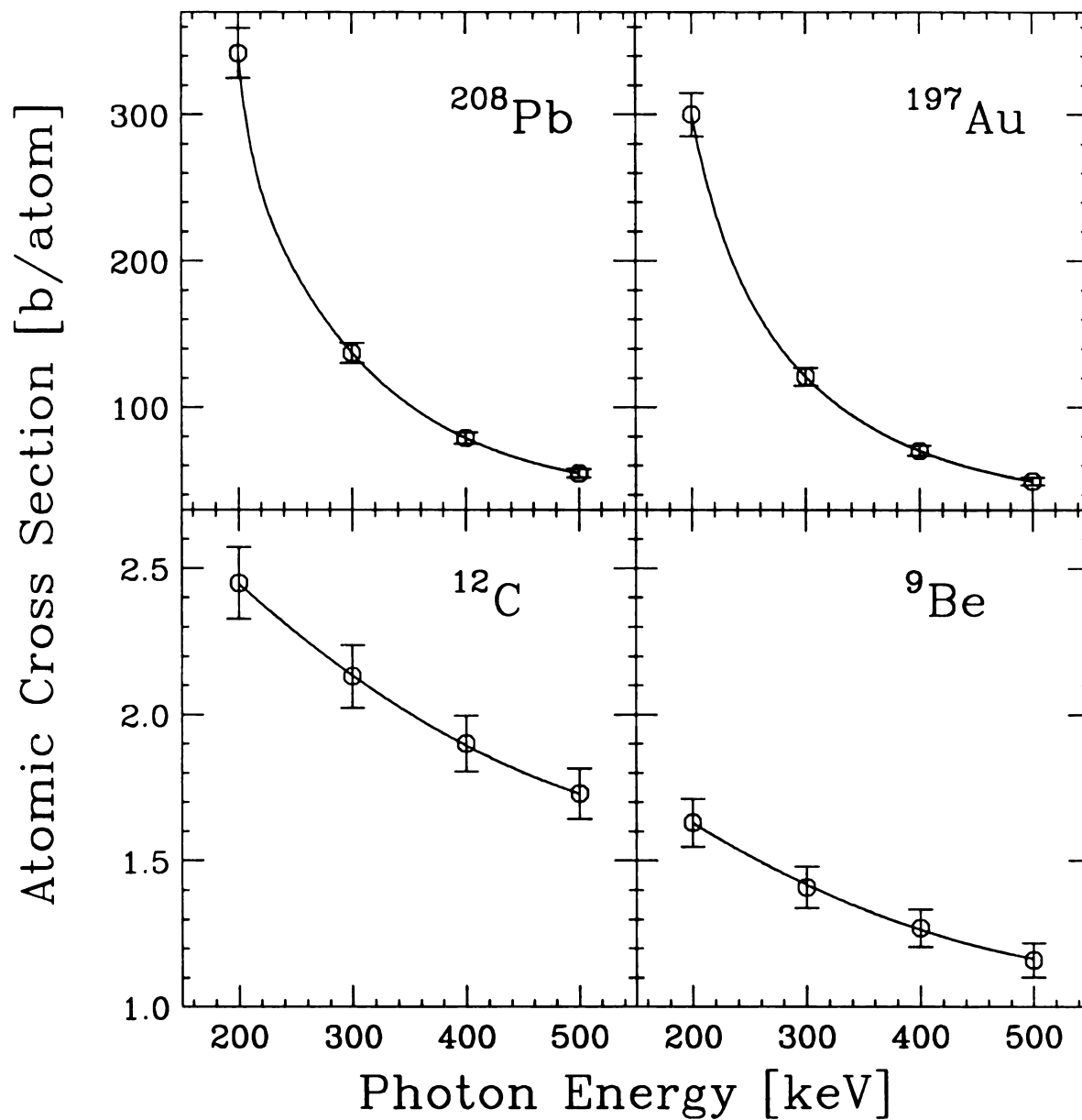
Figure 3.17: Atomic cross sections as a function of photon energy for the four different secondary targets used. The open points represent the data as given in Ref. [Sto70], and the smooth curves show a fit to the data.
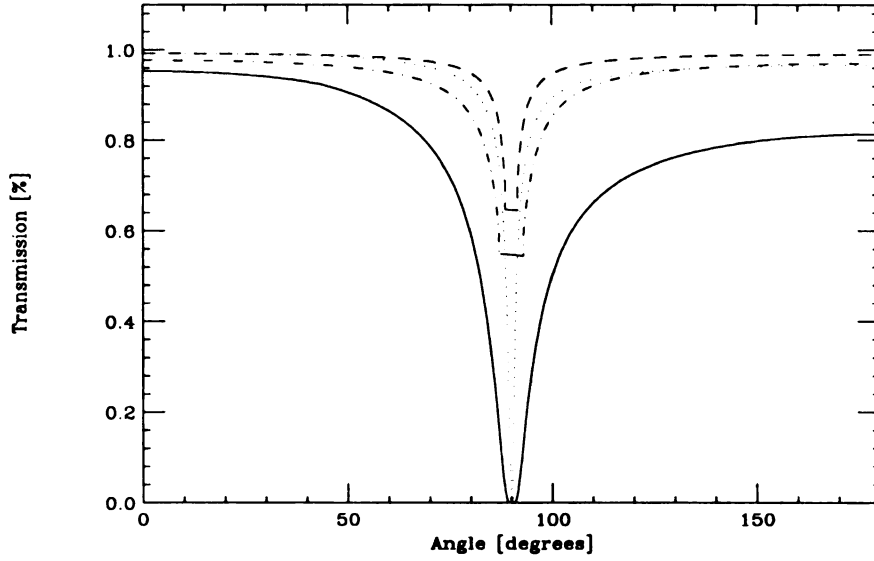
Figure 3.18: Same as Figure 3.16, but now taking the finite target size and the energy dependence of the atomic cross section into account.

Using the same substitution, equation 3.8 expands as follows :

$$I = I_0 \left(1 - \frac{s}{2} + \frac{s^2}{8} - \frac{s^3}{48} \cdots \right) \qquad (3.15)$$

As one can see, the results agree to first order, and the higher order deviations are only small. Our first attempt (using equation 3.8) leads to a slightly lower transmission. In Figure 3.19, a comparison is made between the two different results for the 533 $\frac{mg}{cm^2}$ Au target, which has the strongest absorption and for which the difference in the two approaches should therefore be the largest. The dotted line represents the result calculated by equation 3.13, and the dashed line represents the transmission probability obtained using equation 3.8.

Also shown in Figure 3.19 is the transmission probability as calculated by a linear fit – instead of the third order exponential fit used so far – between the discrete
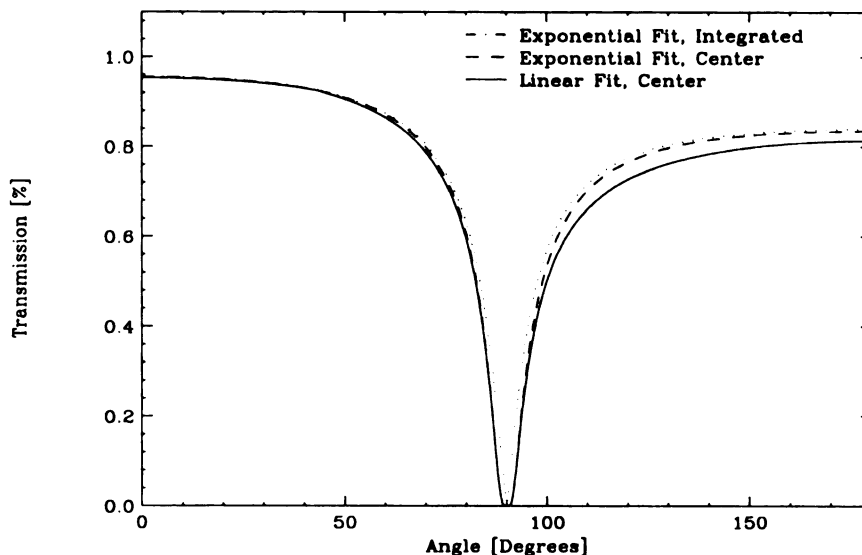
Figure 3.19: Comparison between three different transmission probability calculations for the $533\frac{mg}{cm^2}$ Au target. See text for details.

data points of the atomic cross sections as given by [Sto70]. The difference in the transmission probability from the two interpolation methods was considered and is about 2% in the worst case (gold target). The difference between the three curves in Figure 3.19 can be used to estimate the systematic error we introduce in our cross section calculation. One also has to take the uncertainty in the atomic cross sections into account, which is according to Ref. [Sto70] better than 5%. The systematic error was therefore estimated by using the linear interpolation between the atomic cross section, and the largest possible uncertainty in the atomic cross section. We found the systematic error to be on the order of 5%.

This transmission probability – as calculated with equation 3.13 – has to be combined with the detection efficiency as discussed in the previous chapter. This was done by implementing equation 3.13 into the MATHEMATICA [Mat97] code used to

calculate the detection efficiencies. The modified detection efficiencies and transmission probabilities are given in Table 3.3. As can be seen, the absorption of the low energy γ-ray plays an important role for all targets, and has to be taken into account. Especially for the gold target one would get unreasonable results, if one would ignore the absorption of the photon inside the target material.

Table 3.3: Detection efficiencies for the 320 keV photon, without absorption inside the target material (ϵ_{raw}) and with absorption (ϵ_{corr}), and the transmission probability.

Target		ϵ_{raw} [%]	ϵ_{corr} [%]	Transmission [%]
Pb	$80\frac{mg}{cm^2}$	6.54	5.71	86.7
Au	$533\frac{mg}{cm^2}$	6.55	3.72	56.7
C	$411\frac{mg}{cm^2}$	6.55	5.67	86.5
Be	$195\frac{mg}{cm^2}$	6.55	6.08	92.8

3.3 Experimental Results and Discussion

In the following the results from the experiment will be presented and discussed. For clarity, the experimental results are broken up into three different sections. The first one discusses the Coulomb excitation of ^{11}Be to its first excited state using the ^{208}Pb and the ^{197}Au target. For those targets we are certain to be dealing with Coulomb excitation only, and the results are therefore straightforward to interpret. The measured Coulomb cross sections will be presented, and the B(E1) strength will be derived and compared to previous Coulomb excitation experiments, and to the values deduced from lifetime measurements. The second part also discusses the excitation of ^{11}Be into its first excited state, this time using the light targets (C, Be). In this case one can no longer assume pure Coulomb excitation, but instead a combination of nuclear and Coulomb excitation takes place. The measured cross sections will be compared to model calculations for both the nuclear and Coulomb

excitation processes.

Finally in the third part, the results from the nuclear breakup of ^{11}Be to the first excited state in ^{10}Be are discussed. This process was also observed during the runs on the light targets. From the strength of this transition some information on the ground state wave function of ^{11}Be can be obtained.

3.3.1 ^{11}Be on ^{208}Pb and ^{197}Au targets

The Doppler corrected γ-ray energy spectra for the heavy targets, recorded under the condition that a ^{11}Be fragment was detected in the zero-degree detector ($\theta_{lab} \leq 4.1°$), are shown in Figure 3.20. The two spectra on the top were summed up over the eleven NaI(Tl) detectors that form the inner ring of the NSCL γ-array, whereas the two lower spectra were summed up only over the three detectors we used for the analysis. The counting rates in all spectra are normalized for the particle flux and the number of scattering centers in the various targets. In the projectile frame ($\beta \approx 0.34$) the strong photopeaks centered around a γ-ray energy of 320 keV – corresponding to the $\frac{1}{2}^- \rightarrow \frac{1}{2}^+$ transition in the ^{11}Be projectile – are clearly visible for both the ^{208}Pb and Au targets. The widths of the photopeaks are about 47 keV. According to Table 3.1, this is close to the intrinsic width expected for a 320 keV γ-ray, and shows the effectiveness of the employed Doppler-shift correction. The obvious difference in the yield of the photopeaks measured for the two heavy targets is easily understood by the fact that a fraction of the 320 keV photons are absorbed in the rather thick Au target (see section 3.2.6).

Assuming Rutherford trajectories, we calculate a minimum impact parameter between the heavy targets (Pb, Au) and the ^{11}Be fragments, of approximately 13 fm. This is about 3 fm larger than the distance between the centers of the projectile and target assuming touching spheres, if we neglect the halo character of the ^{11}Be nucleus.
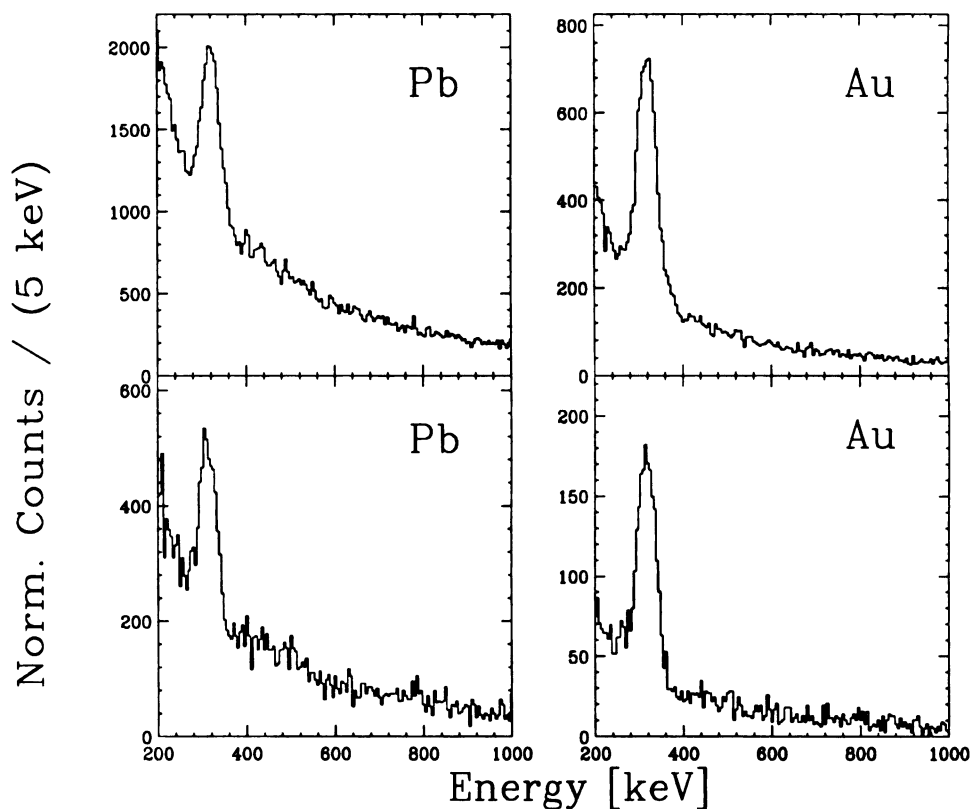
Figure 3.20: Doppler-shift corrected energy spectra for the ^{208}Pb and ^{197}Au secondary targets. The data in the top row were summed up over the eleven detectors that form the inner ring of the NSCL γ-array, whereas the bottom row shows only the data taken with the three detectors used for the analysis. The γ-rays were recorded under the condition that a ^{11}Be fragment was detected in the zero-degree detector. The counting rate is normalized by the incoming particle flux and the number of scattering centers in the various targets.

As mentioned earlier, the extended matter distribution of ^{11}Be may lead to nuclear excitation well beyond distances normally considered safe in Coulomb excitation experiments. However, a comparison between the measured angular distribution of the scattered particles and a coupled channel calculation – using the code ECIS79 [Ray79] – by Nakamura *et al.* [Nak97] show, that nuclear contributions to the cross section in the angular range covered by the zero-degree detector are negligible. As we shall see, this is not true for the light targets (C, Be), where we estimate that the contributions are similar in size from nuclear and Coulomb excitation processes. Therefore, we will treat the heavy and the light targets separately.

The integrated number of beam particles detected in the zero-degree detector ($\theta_{lab} \leq 4.1°$), the number of scattering centers in the various targets, and the number of background subtracted γ-rays in the photopeak provides a relative yield. To determine the Coulomb cross sections, the relative yield was combined with the detector efficiency folded with the angular distribution of the emitted photons (which is isotropic in the projectile rest frame for a $1/2^- \rightarrow 1/2^+$ transition). The absorption of the photons in the different target materials was also taken into account, as already mentioned. Although we included only three NaI(Tl) detectors in the final analysis, the statistics achieved in only a few hours of beam time is sufficient. For the ^{208}Pb target we recorded 1055 ± 95 counts in the background subtracted photopeak within approximately 4.5 hours. For the much thicker ^{197}Au target we recorded 1203 ± 72 counts in the background subtracted photopeak within about 2 hours. From these numbers we extract a Coulomb cross section of (325 ± 39) mb for the ^{208}Pb target, and (257 ± 27) mb for the ^{197}Au target, respectively. The quoted errors take the statistical errors, as well as the uncertainty from the fit/background subtraction, the error from the efficiency calibration, and the error introduced by correcting for the absorption probability – all added in quadrature – into account. The individual

contributions to the total error can be found in Table 3.4.

Table 3.4: The different sources of uncertainty are added in quadrature to yield the total error (see text for details).

Target	Statistical [%]	Fit/Background [%]	Efficiency [%]	Absorption [%]	Total [%]
^{208}Pb	3	9	5	3	11
^{197}Au	3	7	5	5	10

Assuming pure first order Coulomb excitation and the formalism by Winther and Alder [Win79], as introduced in section 3.1 (see also Appendix B), we extracted the reduced transition strength from the measured Coulomb cross sections. We have compared our results to those from the lifetime measurements [Mil83] and to those from the previous two Coulomb excitation experiments [Ann95, Nak97] in Figure 3.21, and in Table 3.3.1. For completeness we show not only the adopted B(E1) value from the lifetime measurement, but also the three experimental results that led to the adopted value. A brief derivation on how the lifetime is connected to the reduced transition strength can be found in Appendix C.

Table 3.5: Measured B(E1) values

Experiment	Ref.	Target	E_{lab} [MeV/nucleon]	B(E1) [e^{2}fm^2]	$\frac{B(E1)_{Lifetime}}{B(E1)_{Coulex}}$ [%]
Lifetime	[Mil83]	–	–	0.116 ± 0.012	–
RIKEN	[Nak97]	^{208}Pb	64	0.099 ± 0.010	85
MSU/NSCL		^{208}Pb	60	0.098 ± 0.011	85
MSU/NSCL		^{197}Au	60	0.082 ± 0.010	71
GANIL	[Ann95]	^{208}Pb	45	0.045 ± 0.006	39
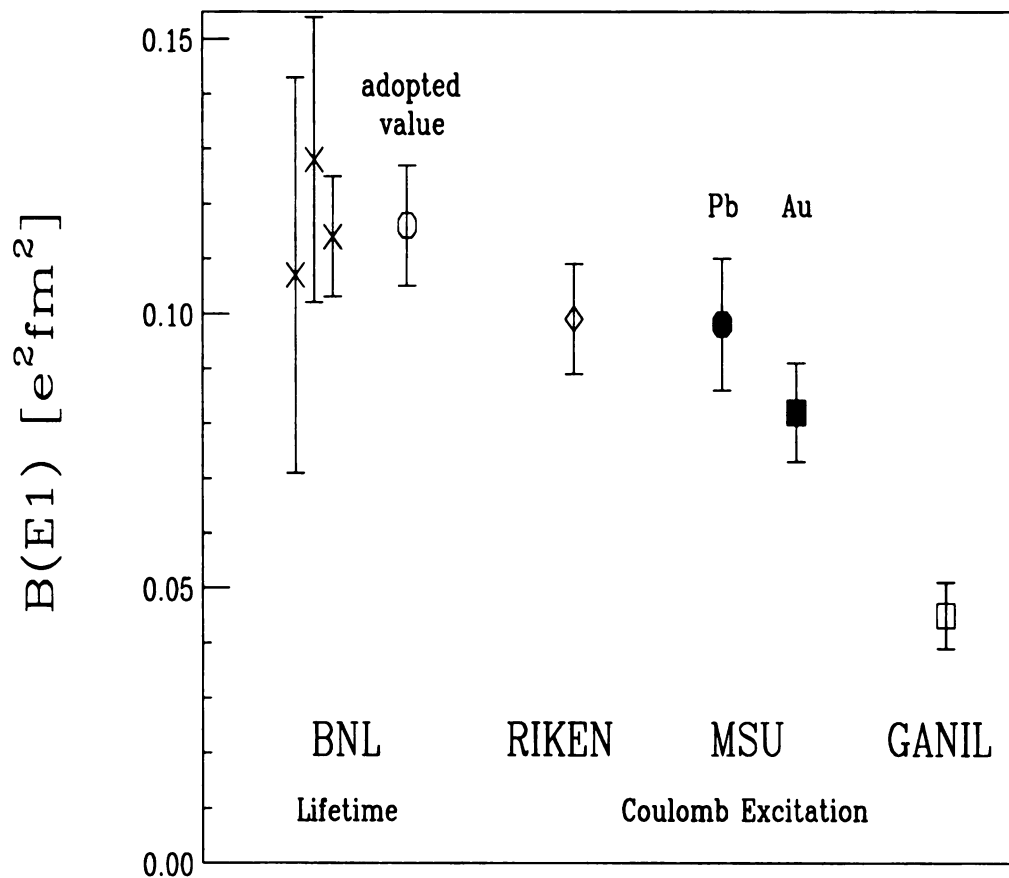
Figure 3.21: Comparison between the different experimentally derived B(E1) values for the $1/2^+ \rightarrow 1/2^-$ transition in ^{11}Be. The results from the lifetime measurements (x) and the adopted value (o) [Mil83] are shown together with the RIKEN measurement (◊) [Nak97] and the GANIL data (□) [Ann95]. The solid symbols represent the present data.

As can be seen in Figure 3.21, the B(E1) value extracted for the gold target is slightly lower than that from the lead target. Recall that large corrections had to be applied to the data from the gold target due to the absorption of the low energy γ-ray inside the target material. As can be seen in Table 3.3 the transmission probability of the low energy γ-ray, for the gold target is, in our simple model, approximately 57%, compared to 87% for the ^{208}Pb target. Uncertainties in the energy dependent absorption coefficients introduce systematic errors in the calculation of the transmission probability which were estimated to be on the order of 5% (see section 3.2.6). However, this error alone can not explain the discrepancy between the measured values, and seems to indicate that we underestimated the absorption in the thick gold target.

In conclusion the extracted value for B(E1) of 0.098(11) e^2fm^2 for the ^{208}Pb target is in excellent agreement with the recent RIKEN result [Nak97]. The extracted B(E1) for the gold target is slightly – but not significantly – lower than the two measurements on the ^{208}Pb targets, and all values agree within error bars. The weighted mean of all three data sets gives a B(E1) of 0.093(6) e^2fm^2. Neither our measurements with several different targets, nor the RIKEN measurement [Nak97] could reproduce the small transition rate from GANIL [Ann95], which also could not be explained by several theoretical models. Both the present B(E1) values and the RIKEN results agree within error bars with the results from the lifetime measurements. The fact that both recent Coulomb excitation experiments only account for about 85% of the adopted B(E1) value extracted from three lifetime measurements indicates that higher order excitation effects, as discussed in Ref. [Typ95, Kid96, Ber95], cannot be excluded by the present data.

3.3.2 ^{11}Be on ^{nat}C and ^{9}Be targets

In Figure 3.22 we show again the Doppler corrected γ-ray energy spectra recorded under the condition that a ^{11}Be fragment was detected in the zero degree-detector, but this time using one of the two light targets. As in the previous section, the spectra on the top were summed up over the eleven NaI(Tl) detectors that form the inner ring of the NSCL γ-array, and the spectra on the bottom show the results for the three detectors we that were used for the analysis. The counting rates were normalized for the particle flux and the number of scattering centers in the various targets. One can clearly see the photopeaks centered around a γ-ray energy of 320 keV – corresponding to the $\frac{1}{2}^- \rightarrow \frac{1}{2}^+$ transition in the ^{11}Be projectile. As expected, the photon yield for the light targets is much smaller than the one for the heavy targets (see Figure 3.20). We obtained photopeaks of similar size for the carbon and the beryllium target. However, for the beryllium target the photopeak is contaminated by a strong background, and the distinction between projectile and background γ-rays becomes difficult. This background is mainly due to nuclear reactions, that were also observed with the other low-Z target. Therefore, the data taken with the beryllium target suffer from large uncertainties in the background subtracted counting rate in the photopeak.

For the low-Z targets we cannot rule out the nuclear contributions to the excitation process. Specifically, the minimum impact parameter insured by the experimental setup for the carbon and beryllium target is smaller than the sum of the radii of the two colliding nuclei. To determine the experimental cross section we followed the same procedure as described in the previous section for the heavy targets. Again we included only three detectors into our final analysis, and again the achieved statistical accuracy is not a limiting factor. We recorded 1173 ± 117 counts in the background
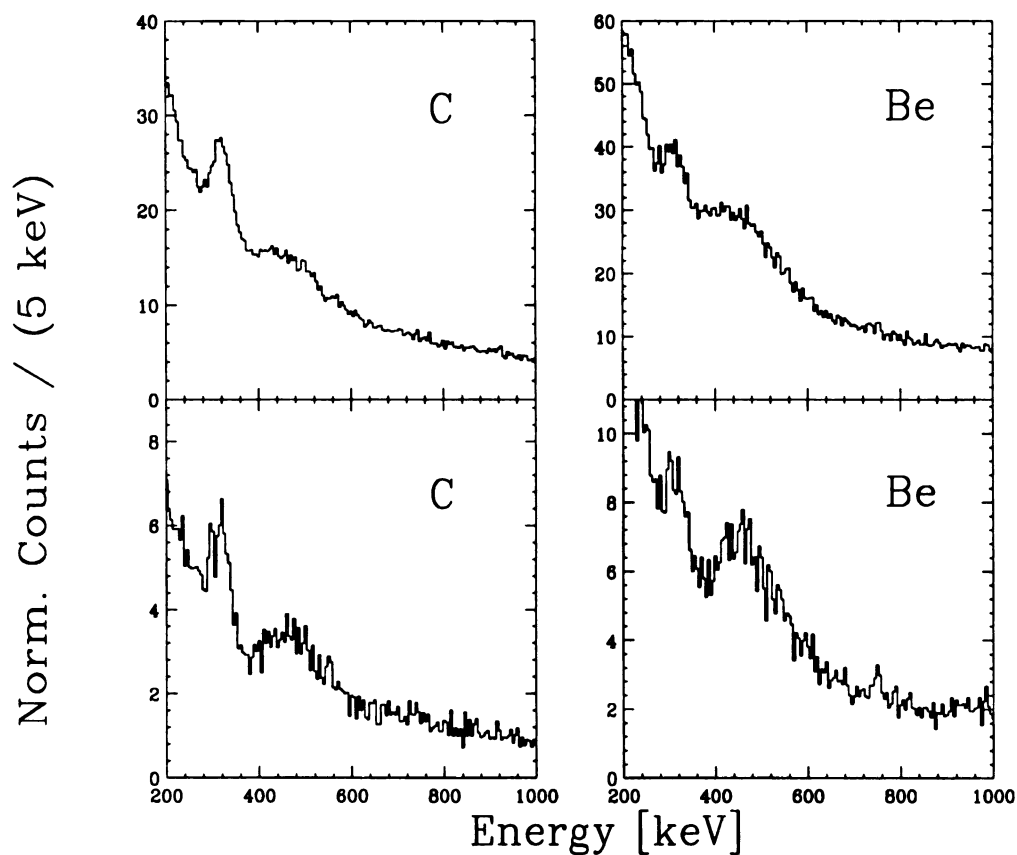
Figure 3.22: Doppler-shift corrected energy spectra for the ^{nat}C and ^{9}Be secondary targets. The data in the top row were summed up over the eleven detectors that form the inner ring of the NSCL γ-array, whereas the bottom row shows only the data taken with the three detectors used for analysis. The γ-rays were recorded under the condition that a ^{11}Be fragment was detected in the zero-degree detector. The counting rate is normalized by the incoming particle flux and the number of scattering centers in the various targets.

subtracted photopeak for the carbon target and about 756 ± 151 counts for the beryllium target. However, as mentioned earlier, because of the large background for the beryllium target, we introduce a rather large error during the fitting/background subtraction process (about 20%). We measured an excitation cross section of (3.4 ± 0.4) mb for the carbon target and (1.8 ± 0.4) mb for the beryllium target. The quoted errors take the statistical errors, as well as the uncertainty from the fit/background subtraction, the error from the efficiency calibration, and the error introduced by correcting for the absorption probability – all added in quadrature – into account. he individual contributions to the total error can be found in Table 3.6.

Table 3.6: The different sources of uncertainty are added in quadrature to yield the total error (see text for details).

Target	Statistical [%]	Fit/Background [%]	Efficiency [%]	Absorption [%]	Total [%]
^{nat}C	3	10	5	3	12
^{9}Be	4	20	5	2	21

These experimentally determined cross sections should be compared to theoretical predictions for the Coulomb and nuclear process. As in the previous section, we calculate the (theoretical) Coulomb cross sections according to Ref. [Win79]. For impact parameters smaller than the sum of the ^{10}Be core and the target radius, one expects core fragmentation to take place, which will not contribute to the state of interest. The energy dependent core and target radii were chosen to reproduce previously measured heavy-ion interaction cross sections [Tan95]. We calculate the minimum impact parameter to be 5.5 (5.2) fm, and accordingly derive a Coulomb cross section of 2.56 (1.15) mb for the carbon (beryllium) target. The measured cross section for the carbon target is about 30% bigger than the theoretical first order

Coulomb excitation cross section. For the beryllium target we measure a 60% larger cross section than predicted by pure first order Coulomb excitation, however, the measured cross section has large uncertainties.

To estimate the nuclear cross section, a similar technique as described in Ref. [Han96] was employed. Again one can assume that all reactions with an impact parameter smaller than the sum of the ^{10}Be core and the target radius result in fragmentation of the core, and therefore can be neglected. Due to the high secondary beam energy one can apply the eikonal approximation, and we assume straight line trajectories for the collision geometry. In the projectile rest frame one can imagine the target nucleus passing through the halo system, without touching the core and leaving a wound in the wave function (see Ref. [Han96] and Appendix D for details). To estimate the nuclear cross section, we have to calculate the overlap of the disturbed ground state wave function with the $l = 1$ wave function from the first excited state. Using Woods-Saxon wave functions, this problem can be solved in the same way as described in Ref. [Han96], and in Appendix D the interested reader can find a short recap of some details of the calculation. We will report only the result of the calculation here. Assuming pure single-particle states, we derive a nuclear cross section of 3.5 mb for the carbon target. If we assume single-particle amplitudes to 0.9 and 0.95 respectively, we get a nuclear cross section of 3 mb for the carbon target. Hence, the theoretically predicted nuclear and Coulomb cross sections are of similar size for the light targets, and comparable to the measured cross section. The fact that the measured cross section is not the sum of the two contributions seems to indicate the presence of Coulomb - nuclear interference.

3.3.3 Nuclear Breakup of ^{11}Be to the First Excited State in ^{10}Be

In the following we will discuss the nuclear breakup of ^{11}Be into the first excited state of ^{10}Be(2^+, 3368 keV) and its subsequent decay to the ^{10}Be(0^+) ground state. This reaction channel was observed during the runs on the carbon and berylium targets. It is of particular interest as one can extract information about the nuclear structure of the ^{11}Be ground state wave function from the strength of this reaction channel. The ground state wave function of ^{11}Be is dominated by the single particle $1s_{1/2}$ intruder state and not – as would be expected from the simple shell model – by the $0p_{3/2}$ state. However, the single particle picture only describes the dominant part of the ground state wave function. One also has to take the coupling of the $0d_{5/2}$ state to the first excited state in the ^{10}Be core into account. Therefore, one can write the ^{11}Be ground state wave function as :

$$|^{11}Be, 1/2^+> = \sqrt{S}|^{10}Be(0^+) \otimes (1s_{1/2})_\nu > +\sqrt{S_d}|^{10}Be(2^+) \otimes (0d_{5/2})_\nu > \quad (3.16)$$

Where S and S_d are the spectroscopic factors. Zwieglinski et $al.$ used the ^{10}Be(d,p)^{11}Be reaction at 25 MeV to extract the spectroscopic factor S to be 0.77 [Zwi79]. Therefore one expects to have about a 20% admixture of $0d_{5/2}$ coupled to the 2^+ core excitation.

Anne et $al.$ measured the dissociation cross section of ^{9}Be(^{11}Be,^{10}Be)n reaction at 41.5 MeV/nucleon to be (290 ± 40) mb [Ann94]. This cross section – properly scaled for the different incident beam energies – can be compared to our cross section for the ^{11}Be → ^{10}Be(2^+) cross section, to extract information about the S_d spectroscopic factor. In principle, the necessary information could also be extracted directly from our data, by comparing the number of incoming ^{11}Be particles to the number of detected ^{10}Be fragments detected in the zero degree detector. This work is currently

in progress. In Fig. 3.23 we show the Doppler corrected γ-ray energy spectra recorded under the condition that a ^{10}Be fragment was detected in the zero degree-detector for the 195 $\frac{mg}{cm^2}$ target. The spectra were summed up over the same three detectors used for the previous analysis to assure a well defined efficiency calibration. The spectrum on the left hand side of Figure 3.23 was recorded under the additional condition that only one γ-ray was detected (multiplicity = 1). By multiplicity we mean the number of simultaneously detected γ-rays in the NSCL γ-array, and not the multiplicity of actually emitted γ-rays. The quantity we call multiplicity is also often referred to as fold. A photopeak at an energy of 3368 keV is clearly visible, as is the first escape peak, located 511 keV lower in energy. The spectrum on the right hand side of Figure 3.23 does not use the additional multiplicity cut, in other words many γ-rays could be detected simultaneously. One can clearly see the increase in background counts. In Figure 3.24 we show the same spectra for the 411 $\frac{mg}{cm^2}$ target. Again, we plot the spectrum with the multiplicity cut on the left hand side. Although, the photopeak at 3368 keV is still clearly visible, the background – even in the spectrum with the multiplicity cut – is much higher, due to target γ-rays.

We now have to discuss the influence of the multiplicity – or fold – cut on the observed γ-ray yield. In Figure 3.25 we show the background subtracted counting rate in the 3368 keV photopeak as a function of observed γ-ray multiplicity for the carbon target. One can clearly see, that the counting rate depends on the multiplicity cut. Therefore, one has to use the spectrum without the multiplicity – or fold – cut to evaluate the γ-ray yield. This introduces an additional error, as it is much harder to get a reliable background subtracted peak from each of those spectra.

We recorded 1230 ± 188 counts in the background subtracted photopeak for the berylium target, and 1195 ± 203 counts for the carbon target. Combining the γ-ray yield with the number of beam particles detected in the zero-degree detector, and
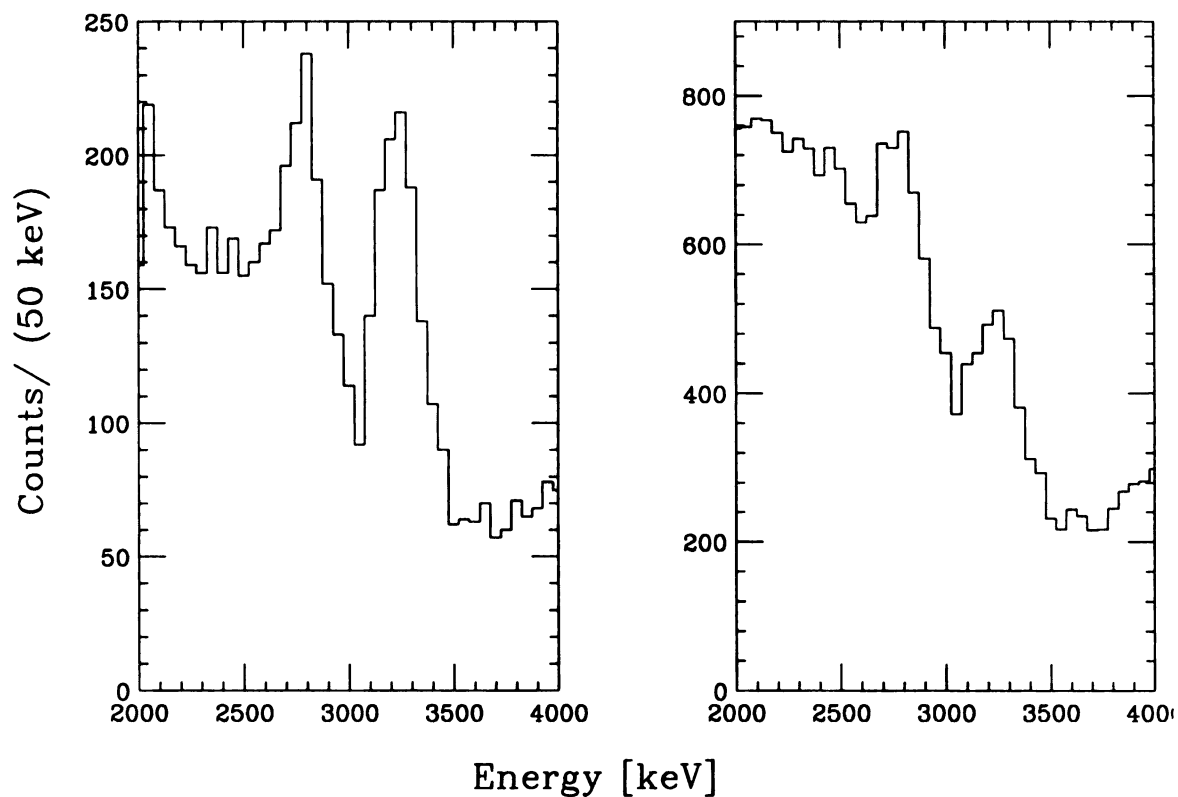
Figure 3.23: Doppler-shift corrected energy spectra for the ^{9}Be secondary target.The data were recorded under the condition that a ^{10}Be fragment was detected in the zero-degree detector. The spectrum on the left hand side has the additional requirement of only a single detected γ-ray.
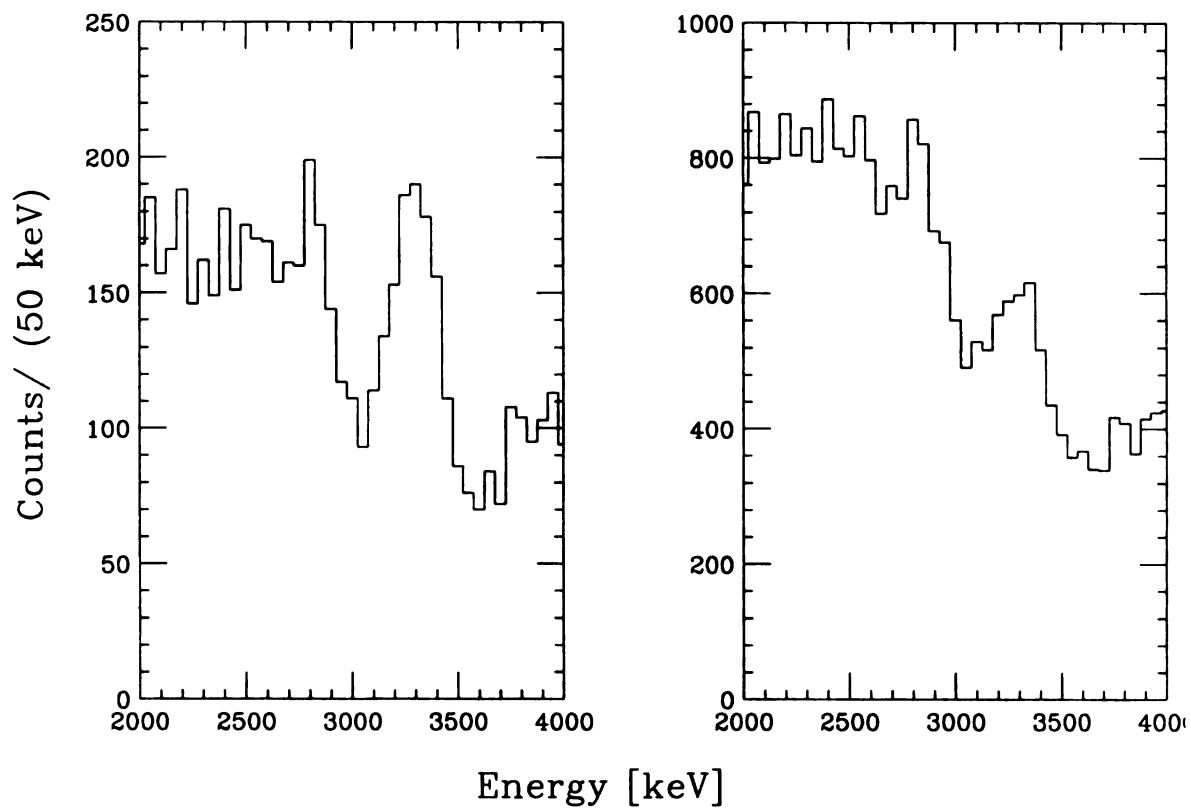
Figure 3.24: Doppler-shift corrected energy spectra for the ^{nat}C secondary target. The data were recorded under the condition that a ^{10}Be fragment was detected in the zero-degree detector. The spectrum on the left hand side has the additional requirement of only a single detected γ-ray.
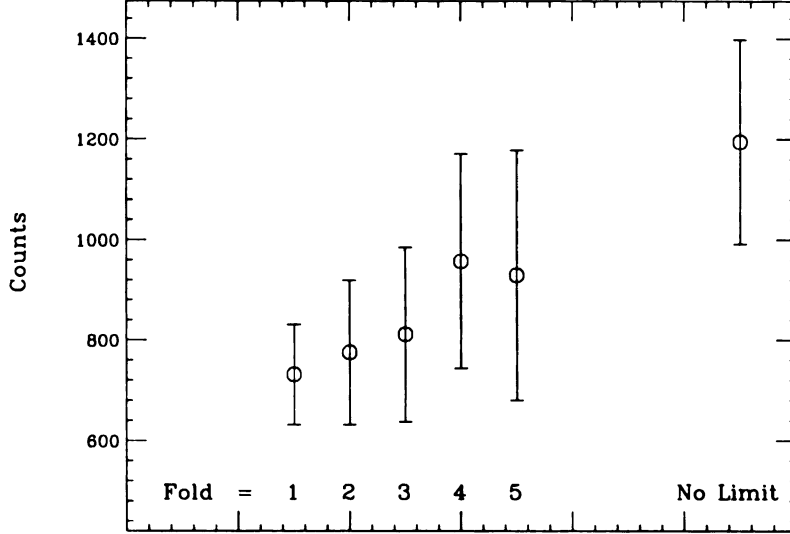
Figure 3.25: Background subtracted counting rate in the 3368 keV photopeak as a function of detected γ-ray multiplicity – or fold – for the carbon target.

the number of scattering centers in the various targets provides a relative yield. To determine the cross section, one has to combine this information with the detector efficiency folded with the angular distribution of the emitted photons, where one has to take the population of the m-substates into account as well. The later was done by using the formalism as described in Ref. [Win79] (see also Ref. [Sch97]). We extract a cross section of (34.5 ± 8) mb for the berylium target, and a cross section of (22.1 ± 6) mb for the carbon target. The quoted errors take the statistical errors, as well as the uncertainty from the fit/background subtraction, and the error from the efficiency calibration – all added in quadrature – into account.

As mentioned earlier, these cross sections have to be compared to the total dissociation cross section as measured by Anne *et al.* [Ann94]. However, as their data were taken at a lower incident beam energy, namely 45.1 MeV/nucleon compared to our data taken at 60.1 MeV/nucleon, we first have to scale the measured total dissociation cross section accordingly. If we assume that the dissociation cross section

scales like the free neutron-neutron (n-n) cross section, we have to reduce the value of (290 ± 40) mb to (221 ± 31) mb. Therefore, our measured cross section for the nuclear breakup of ^{11}Be to the first excited state in ^{10}Be is about (16 ± 4) % of that of the total dissociation channel.

Chapter 4

Summary and Outlook

The present work studied the structure of light neutron-rich nuclei. Especially the knowledge about the exact location of the neutron dripline was extended for the oxygen isotopes. Using the measured cross sections of the lighter oxygen isotopes, we predict that several hundred events of ^{26}O should have been observed. However, we could not attribute a single event to the production of ^{26}O. An upper limit on the production cross section for ^{26}O of 7 pb at a 90% confidence level was determined. As large effort was put into assuring that the particles of interest were centered at both the intermediate and final focus of the A1200, this result indicates that the lifetime of ^{26}O must indeed be appreciably shorter than the central flight time through the separator (approximately 188 ns). This result indicates that ^{26}O is not particle stable, and that ^{24}O is, in fact, the heaviest bound oxygen isotope. The finding that ^{26}O is particle unbound provides another very stringent test to the predictions of theoretical models. During the search for ^{26}O the production cross sections of 72 neutron-rich nuclei, ranging from ^{38}P to ^{11}B, were also determined and compared to model predictions.

In the second part of the present work, the technique of intermediate energy projectile Coulomb excitation was employed to study the one-neutron halo nucleus ^{11}Be.

The measurement of the excitation cross section of ^{11}Be from its $\frac{1}{2}^+$ ground state to the $\frac{1}{2}^-$ first excited state on both light and heavy targets allowed us to investigate the various contributions to the excitation cross section. The extracted reduced transition strength B(E1) for the lead and gold target agrees with a previous Coulomb excitation measurement from RIKEN [Nak97] on a lead target. Those measurements account for about 80% of the B(E1) extracted from a lifetime measurement [Mil83]. This indicates that higher order excitation effects, as discussed in Ref. [Typ95, Kid96, Ber95], cannot be excluded by the present data. Neither the present work, nor the RIKEN measurement could reproduce the small transition rate reported from a GANIL measurement [Ann95].

For the carbon and berylium targets we predict a contribution of similar size from the Coulomb and nuclear excitation channels to the measured cross section. From the fact that the measured excitation cross section is not the sum of the predicted Coulomb and nuclear processes, we deduce that Coulomb-nuclear interference plays a role.

The nuclear breakup of ^{11}Be into the first excited state of ^{10}Be(2^+, 3368 keV) and its subsequent decay to the ^{10}Be(0^+) ground state was also observed during the runs on the carbon and berylium targets. The measured cross section for the nuclear breakup of ^{11}Be to the first excited state in ^{10}Be accounts for about (16 ± 4) % of that from the total dissociation channel [Ann94], if the later is properly scaled for the different incident energies. This result is in good agreement with the measured spectroscopic factor of 0.77 from the ^{10}Be(d,p)^{11}Be reaction at 25 MeV [Zwi79], and confirms the dominant single particle character of the ^{11}Be ground state.

For an outlook into the future, one can say that although the knowledge and understanding of light neutron-rich nuclei has increased tremendously in recent years,

much work still remains to be done. The recently commissioned S800 spectrograph, as well as the planned new radioactive beam facilities at MSU and RIKEN will provide the opportunity to study light neutron-rich nuclei in more detail. The availability of much increased beam intensities will allow one not only to expand the knowledge about the exact location of the driplines even further, but also provide sufficient secondary beam intensities for detailed nuclear structure studies.

APPENDICES

Appendix A

Measured Cross Sections

The following tables show the the individual measured cross sections for 72 neutron-rich isotopes ranging from ^{38}P to ^{11}B, together with the predictions from the EPAX parameterization [Süm90]. The listed uncertainty takes the statistical error, as well as the uncertainty from the gaussian fit to to the momentum distributions – both added in quadrature – into account.

Table A.1: Isotopic cross sections from the reaction ^{40}Ar + ^{9}Be at 90 MeV/nucleon.

Z	A	σ_{EPAX} [mb]	σ_{EXP} [mb]
15	38	$4.18 \cdot 10^{-03}$	$(4.55 \pm .42) \cdot 10^{-02}$
15	37	$2.55 \cdot 10^{-01}$	$(1.18 \pm .08) \cdot 10^{+00}$
15	36	$1.16 \cdot 10^{+00}$	$(1.87 \pm .07) \cdot 10^{+00}$
15	34	$1.17 \cdot 10^{+01}$	$(2.15 \pm .1) \cdot 10^{+00}$
14	37	$3.24 \cdot 10^{-04}$	$(1.34 \pm .21) \cdot 10^{-03}$
14	36	$2.47 \cdot 10^{-02}$	$(1.68 \pm .20) \cdot 10^{-02}$
14	35	$1.39 \cdot 10^{-01}$	$(8.40 \pm .79) \cdot 10^{-02}$
14	34	$6.19 \cdot 10^{-01}$	$(7.56 \pm .38) \cdot 10^{-01}$
14	33	$2.35 \cdot 10^{+00}$	$(1.21 \pm .03) \cdot 10^{+00}$
14	32	$7.41 \cdot 10^{+00}$	$(1.34 \pm .08) \cdot 10^{+00}$
13	35	$1.95 \cdot 10^{-03}$	$(1.05 \pm .11) \cdot 10^{-03}$
13	34	$1.22 \cdot 10^{-02}$	$(1.02 \pm .09) \cdot 10^{-02}$
13	33	$6.69 \cdot 10^{-02}$	$(1.97 \pm .11) \cdot 10^{-01}$
13	32	$3.23 \cdot 10^{-01}$	$(6.59 \pm .39) \cdot 10^{-01}$
13	31	$1.34 \cdot 10^{+00}$	$(2.11 \pm .06) \cdot 10^{+00}$
13	30	$4.67 \cdot 10^{+00}$	$(1.76 \pm .07) \cdot 10^{+00}$
13	29	$1.29 \cdot 10^{+01}$	$(3.89 \pm .35) \cdot 10^{+00}$
12	33	$8.08 \cdot 10^{-04}$	$(3.50 \pm .53) \cdot 10^{-04}$
12	32	$5.38 \cdot 10^{-03}$	$(8.05 \pm .89) \cdot 10^{-03}$
12	31	$3.22 \cdot 10^{-02}$	$(5.92 \pm .57) \cdot 10^{-02}$
12	30	$1.70 \cdot 10^{-01}$	$(4.18 \pm .25) \cdot 10^{-01}$
12	29	$7.71 \cdot 10^{-01}$	$(9.09 \pm .42) \cdot 10^{-01}$
12	28	$2.93 \cdot 10^{+00}$	$(1.03 \pm .04) \cdot 10^{+00}$
12	27	$8.90 \cdot 10^{+00}$	$(3.76 \pm .35) \cdot 10^{+00}$
11	31	$3.31 \cdot 10^{-04}$	$(3.61 \pm .56) \cdot 10^{-04}$
11	30	$2.40 \cdot 10^{-03}$	$(3.50 \pm .35) \cdot 10^{-03}$
11	29	$1.56 \cdot 10^{-02}$	$(5.32 \pm .26) \cdot 10^{-02}$
11	28	$8.98 \cdot 10^{-02}$	$(3.87 \pm .15) \cdot 10^{-01}$
11	27	$4.44 \cdot 10^{-01}$	$(1.93 \pm .07) \cdot 10^{+00}$
11	26	$1.84 \cdot 10^{+00}$	$(3.00 \pm .09) \cdot 10^{+00}$
11	25	$6.11 \cdot 10^{+00}$	$(4.43 \pm .42) \cdot 10^{+00}$
10	28	$1.09 \cdot 10^{-03}$	$(1.75 \pm .16) \cdot 10^{-03}$
10	27	$7.69 \cdot 10^{-03}$	$(5.95 \pm .48) \cdot 10^{-03}$
10	26	$4.79 \cdot 10^{-02}$	$(2.61 \pm .11) \cdot 10^{-01}$
10	25	$2.57 \cdot 10^{-01}$	$(1.12 \pm .06) \cdot 10^{+00}$
10	24	$1.16 \cdot 10^{+00}$	$(3.90 \pm .16) \cdot 10^{+00}$
10	23	$4.19 \cdot 10^{+00}$	$(4.02 \pm .20) \cdot 10^{+00}$
10	22	$1.15 \cdot 10^{+01}$	$(3.65 \pm .36) \cdot 10^{+00}$

Table A.2: Isotopic cross sections from the reaction ^{40}Ar + ^{9}Be at 90 MeV/nucleon.

Z	A	σ_{EPAX} [mb]	σ_{EXP} [mb]
9	26	$5.00 \cdot 10^{-04}$	$(3.52 \pm .60) \cdot 10^{-04}$
9	25	$3.84 \cdot 10^{-03}$	$(1.19 \pm .12) \cdot 10^{-02}$
9	24	$2.59 \cdot 10^{-02}$	$(1.00 \pm .08) \cdot 10^{-01}$
9	23	$1.50 \cdot 10^{-01}$	$(1.55 \pm .08) \cdot 10^{+00}$
9	22	$7.32 \cdot 10^{-01}$	$(3.29 \pm .13) \cdot 10^{+00}$
9	21	$2.88 \cdot 10^{+00}$	$(7.48 \pm .30) \cdot 10^{+00}$
9	20	$8.58 \cdot 10^{+00}$	$(3.75 \pm .18) \cdot 10^{+00}$
8	24	$2.33 \cdot 10^{-04}$	$(3.56 \pm .35) \cdot 10^{-04}$
8	23	$1.94 \cdot 10^{-03}$	$(1.40 \pm .12) \cdot 10^{-03}$
8	22	$1.42 \cdot 10^{-02}$	$(8.16 \pm .65) \cdot 10^{-02}$
8	21	$8.89 \cdot 10^{-02}$	$(6.41 \pm .39) \cdot 10^{-01}$
8	20	$4.67 \cdot 10^{-01}$	$(4.18 \pm .20) \cdot 10^{+00}$
8	19	$1.98 \cdot 10^{+00}$	$(5.85 \pm .22) \cdot 10^{+00}$
8	18	$6.42 \cdot 10^{+00}$	$(6.44 \pm .26) \cdot 10^{+00}$
7	22	$1.11 \cdot 10^{-04}$	$(3.45 \pm .52) \cdot 10^{-04}$
7	21	$9.97 \cdot 10^{-04}$	$(8.05 \pm .89) \cdot 10^{-03}$
7	20	$7.85 \cdot 10^{-03}$	$(3.82 \pm .36) \cdot 10^{-02}$
7	19	$5.31 \cdot 10^{-02}$	$(6.20 \pm .50) \cdot 10^{-01}$
7	18	$3.01 \cdot 10^{-01}$	$(2.08 \pm .08) \cdot 10^{+00}$
7	17	$1.37 \cdot 10^{+00}$	$(7.26 \pm .29) \cdot 10^{+00}$
7	16	$4.81 \cdot 10^{+00}$	$(5.54 \pm .22) \cdot 10^{+00}$
7	15	$1.16 \cdot 10^{+01}$	$(4.51 \pm .31) \cdot 10^{+00}$
6	19	$5.21 \cdot 10^{-04}$	$(1.75 \pm .35) \cdot 10^{-03}$
6	18	$4.43 \cdot 10^{-03}$	$(4.48 \pm .76) \cdot 10^{-02}$
6	17	$3.22 \cdot 10^{-02}$	$(8.93 \pm .89) \cdot 10^{-02}$
6	16	$1.96 \cdot 10^{-01}$	$(1.33 \pm .08) \cdot 10^{+00}$
6	15	$9.62 \cdot 10^{-01}$	$(3.40 \pm .20) \cdot 10^{+00}$
6	14	$3.62 \cdot 10^{+00}$	$(1.62 \pm .09) \cdot 10^{+01}$
6	13	$9.47 \cdot 10^{+00}$	$(5.34 \pm .27) \cdot 10^{+00}$
5	15	$1.98 \cdot 10^{-02}$	$(1.08 \pm .24) \cdot 10^{-01}$
5	14	$1.29 \cdot 10^{-01}$	$(1.59 \pm .27) \cdot 10^{-01}$
5	13	$6.81 \cdot 10^{-01}$	$(2.55 \pm .25) \cdot 10^{+00}$
5	12	$2.74 \cdot 10^{+00}$	$(5.28 \pm .32) \cdot 10^{+00}$
5	11	$7.73 \cdot 10^{+00}$	$(5.75 \pm .30) \cdot 10^{+00}$

Appendix B

The Coulomb excitation process

The Coulomb excitation process can be evaluated in a semi-classical picture as developed by Winther and Alder [Win79]. In this case, one assumes that the motion takes place along classical Rutherford trajectories, and that the excitation process itself can be described via quantum mechanical perturbation theory. This of course is only possible for weak excitations. The cross section for exciting a final state $|f>$ from the initial state $|i>$ is given by :

$$\frac{d\sigma}{d\Omega} = \left(\frac{d\sigma}{d\Omega}\right)_{Ruth} P_{if} \tag{B.1}$$

The Rutherford cross section is expressed by :

$$\left(\frac{d\sigma}{d\Omega}\right)_{Ruth} = \frac{a_0^2}{4sin^4(\frac{\theta}{2})} \tag{B.2}$$

here θ is the scattering angle and $2 \cdot a_0$ is the distance of closest approach, which can be calculated as :

$$a_0 = \frac{Z_T Z_P e^2}{m_0 c^2 \beta^2} \tag{B.3}$$

where, $Z_{T,P}$ is the elemental number of the target (projectile) respectively, m_0 is the

reduced mass of the system, and c^2 is the square of the speed of light. For reactions with incident energies below the Coulomb barrier, the minimum a_0 is achieved for central collisions.

P_{if} is the probability to excite the state $|f>$, and for weak excitations it can be expressed via first order perturbation theory as :

$$P_{if} = |a_{if}|^2 \qquad (B.4)$$

where the transition amplitude a_{if} can be expressed as :

$$a_{if} = \frac{1}{i\hbar} \int_{-\infty}^{\infty} e^{i\omega_{fi}t} < f|V(\mathbf{r}(t))|i > dt \qquad (B.5)$$

Here, $V(\mathbf{r}(t))$ is the time-dependent electromagnetic potential, that is given by the Liénard-Wiechert potential, and ω_{fi} is given by $\omega_{fi} = \frac{1}{\hbar}(E_f - E_i)$.

One can expand the electromagnetic potential $V(\mathbf{r}(t))$ in its multipole components $V_{\lambda\mu}(\mathbf{r}(t))$, and express the transition amplitude a_{if} in terms of the electric and magnetic multipole moments $M(E\lambda\mu)$ and $M(M\lambda\mu)$ – or in general $M(\pi\lambda\mu)$ – respectively as :

$$a_{if} = i \sum_{\lambda} \frac{Z_T e < f|M(\pi\lambda\mu)|i >}{\hbar c a_0^{\lambda}} f_{\lambda}(\zeta) \qquad (B.6)$$

Here, $f_{\lambda}(\zeta)$ is a function that depends on the adiabaticity parameter which, for non-relativistic energies, is given by :

$$\zeta = \omega_{fi}\tau_{coll} = \omega_{fi}\frac{a_0}{v} \qquad (B.7)$$

where τ_{coll} is the collision time, which is given by $\tau_{coll} = \frac{a_0}{v}$, where v is the projectile

velocity, and $2 \cdot a_0$ is the distance of closest approach, given by equation B.3. For $\zeta > 1$ the collision is adiabatic and the excitation probability falls exponentially with ζ. Therefore, the adiabatic cutoff is given for $\zeta \approx 1$, and this limits the possible excitation energies to about 1-2 MeV (see equation B.7).

For intermediate and relativistic energies equation B.7 needs to be slightly modified. For reactions with incident beam energies below the Coulomb barrier, the distance of closest approach was reached for central collisions. For higher incident beam energies, one only can consider pure Coulomb excitation, if the impact parameter (b) of the colliding system is larger than the sum of the radii of the two nuclei. One also has to take the Lorentz contraction of the electromagnetic field into account, so that the adiabaticity parameter for relativistic energies should be written as :

$$\zeta = \omega_{fi} \tau'_{coll} = \omega_{fi} \frac{b}{v\gamma} \tag{B.8}$$

where γ is the usual relativistic factor ($\gamma = 1/\sqrt{1-\beta^2}, \beta = \frac{v}{c}$). Due to the shorter collision time τ'_{coll} in intermediate and relativistic energy collisions, the adiabaticity parameter is smaller than in the above discussed non-relativistic collisions. Therefore, the maximum reachable excitation energy is also larger at those higher incident beam energies.

One can now write the Coulomb cross section for exciting a state $|f>$ with λ-pole pure Coulomb excitation as :

$$\sigma_\lambda = 2\pi \int_{b_0}^{b_{adiab}} \left| \frac{Z_T e < f|M(\pi\lambda\mu)|i >}{\hbar c b^\lambda} \right|^2 b\,db \tag{B.9}$$

where the lower integration limit is the minimum impact parameter, given by the sum of the two nuclear radii, and the upper integration limit is given by the impact parameter at which the adiabaticity parameter ζ (see equation B.8) is equal to unity

(adiabatic cutoff). This integral can be evaluated using first order time-dependent perturbation theory. A detailed discussion about this subject can be found in Ref. [Win79], and goes well beyond the scope of this work. Therefore, we will only quote the final result, which relates the Coulomb excitation cross section to the reduced transition strength $B(\pi\lambda)$, namely :

$$\sigma_{coul} = \left(\frac{Z_T e^2}{\hbar c}\right)^2 \sum_{\pi\lambda\mu} k^{2(\lambda-1)} \frac{1}{e^2} B(\pi\lambda) |G_{\pi\lambda\mu}(\frac{v}{c})|^2 g_\mu(\zeta(b_{min})) \qquad (B.10)$$

where the functions $G_{\pi\lambda\mu}$ are tabulated in Ref. [Win79], and the functions $g_\mu(\zeta)$ can be expressed via the modified Bessel functions (K_μ) as :

$$g_\mu(\zeta) = g_{-\mu}(\zeta) = \pi\zeta^2[|K_{\mu+1}(\zeta)|^2 - |K_\mu(\zeta)|^2 - \frac{2\mu}{\zeta}K_{\mu+1}(\zeta)K_\mu(\zeta)] \qquad (B.11)$$

In our case, we are interested in an electric dipole transition from the first excited state to the ground state in ^{11}Be. Therefore, the above general equation will simplify for our special application to :

$$\sigma_{coul} = \left(\frac{Z_T e^2}{\hbar c}\right)^2 \frac{B(E1)}{e^2} \frac{16\pi}{9}[g_1(\zeta) + (1 - \beta^2)g_0(\zeta)] \qquad (B.12)$$

It should be pointed out here, that the adiabaticity parameter is specific for each experiment, as it depends on the beam energy and on the minimum impact parameter which depends on the experimental setup. One can express the minimum impact parameter as :

$$b_0 = \frac{a_0}{\gamma}cot\left(\frac{1}{2}\theta_{max}\right) \qquad (B.13)$$

Here, a_0 is given by equation B.3, γ is the usual relativistic parameter, and the

maximum scattering angle θ_{max} is given by the experimental setup ($\theta_{max} = 4.1°$ in our case).

Appendix C

Nuclear Transition Matrix Elements

In the following, I will briefly describe, how one can derive the reduced transition strength B(Eλ) – where λ denotes the multipolarity of the transition – from the measured lifetime. Many intermediate steps in the derivation are left out, and for a more detailed description of this subject, the interested reader should refer to, e.g. the textbook of Wong [Won90].

The measured lifetime T, the half-life $T_{1/2}$ and the transition probability P are related via :

$$T = \frac{T_{1/2}}{ln2} = \frac{1}{P} \tag{C.1}$$

For weak interactions, one can use first oder time-dependent perturbation theory to derive Fermi's golden rule, which relates the transition probability to the square of the nuclear matrix element M_{fi} :

$$\begin{aligned} P &= \frac{2\pi}{\hbar} | < J_f M_f \zeta |H'| J_i M_i \xi > |^2 \rho(E_f) \\ &= \frac{2\pi}{\hbar} |M_{fi}|^2 \rho(E_f) \end{aligned} \tag{C.2}$$

Here $\rho(E_f)$ is the final state level density per energy interval at the energy E_f, and $|J_i M_i \xi >$ and $|J_f M_f \zeta >$ are the wave functions of the initial and final states. H' represents the perturbation due to the coupling between the nuclear and electromagnetic fields, and ζ, ξ denote quantum numbers other than the angular momentum, that are necessary to describe the nuclear states. One can expand the perturbing Hamiltonian H' in multipoles λ, μ, as shown e.g. in [Won90], and write the electric part of H' as :

$$\mathbf{O}_{\lambda\mu}(E\lambda) = -\frac{i(2\lambda + 1)!!}{ck^{\lambda+1}(\lambda + 1)}\mathbf{J}(\mathbf{r})\nabla \times (\mathbf{r} \times \nabla)(j_\lambda(kr)Y_{\lambda\mu}(\theta, \phi)) \qquad (C.3)$$

where the nuclear current density is given by $\mathbf{J}(\mathbf{r})$, and $j_\lambda(kr)$ are the spherical Bessel functions and $Y_{\lambda\mu}(\theta, \phi)$ are the spherical harmonics.

The reduced nuclear matrix element is related to the reduced transition strength $B(\lambda)$ – for a given multipolarity λ – via the following relation :

$$B(\lambda) = \sum_{\mu M_f} | < J_f M_f \zeta |\mathbf{O}_{\lambda\mu}|J_i M_i \xi > |^2 \qquad (C.4)$$

$$= \frac{1}{2J_i + 1}| < J_f\zeta||\mathbf{O}_\lambda||J_i\xi > |^2 \qquad (C.5)$$

After including the level density of the final states, one can now express the transition rate $P(E\lambda)$ –given by equation C.2 – in relation to the reduced transition strength B(Eλ) for electric transitions via the relation :

$$P(E\lambda) = \alpha\hbar c\frac{8\pi(\lambda + 1)}{\lambda[(2\lambda + 1)!!]^2}\frac{1}{\hbar}(\frac{1}{\hbar c})^{2\lambda+1}E_\gamma^{2\lambda+1}B(E\lambda) \qquad (C.6)$$

Here, E_γ is given in MeV, and B(Eλ) in units of $e^2 fm^{2\lambda}$. For the E1 transition we are interested in, one can combine the constants in equation C.6 and end up with

the following formula :

$$P(E1) = 1.59 \cdot 10^{15} E_\gamma^3 B(E1) \qquad \text{(C.7)}$$

Again, E_γ is given in MeV, and B(E1) in units of $e^2 fm^2$. Using equation C.7 in combination with equation C.1, and the measured lifetimes as given in Ref. [Mil83], we deduce the B(E1) values as shown in Fig. 3.21.

Appendix D

Transition Amplitude for the Nuclear Excitation in ^{11}Be

To calculate the nuclear excitation of ^{11}Be from its $\frac{1}{2}^{+}$ ground state to the $\frac{1}{2}^{-}$ first excited state, we will follow closely the model developed by P.G. Hansen to describe the momentum content of a single-nucleon halo state [Han96, Han97]. Due to the relative high energy of the secondary beam, one can use the classical impact parameter (b) and straight line trajectories to describe the colliding system. Only reactions with a minimum impact parameter (b_{min}) larger than the sum of the projectile core radius (R_C) and the target radius (R_T) can contribute to the reaction channel of interest. Reactions with a smaller impact parameter will lead to core fragmentation. The minimum impact parameter can be calculated as :

$$
\begin{aligned}
b_{min} &= R_C + R_T \\
&= r_0 \cdot \left(A_C^{1/3} + A_T^{1/3} \right) \\
&= (1.7718 - 0.13036 \cdot ln[E_{beam}]) \cdot \left(A_C^{1/3} + A_T^{1/3} \right) \quad\quad \text{(D.1)}
\end{aligned}
$$

Where $A_{C,T}$ are the core and target masses, and we used the energy dependent core and target radii according to Ref. [Tan95].

In the projectile rest frame, one can imagine the target nucleus passing through the halo system without touching the core, but leaving a wound in the undisturbed ground state wave function (Ψ_0). The size of the wound is determined by the range of the interaction, which one can describe by an effective target radius (R_a). Figure D.1 shows a sketch of the coordinate system and the relevant parameters used. Therefore, the wave function Ψ_0 remains unchanged, except in a cylinder of radius R_a, where it is set to zero. We call the wave function originally contained in this reaction zone $\delta\Psi_0$. This wave function vanishes outside the interaction radius R_a, and it can be chosen to reproduce the experimental reaction and elastic cross section for free nucleons. One can express the collision complex ($\Psi(\mathbf{r})$) as the sum of the undisturbed ground state wave function and the wound as :

$$\Psi(\mathbf{r}) = \Psi_0 - \delta\Psi_0 \tag{D.2}$$

To estimate the nuclear cross section, one has to calculate the overlap of this wave function with the $l = 1$ wave function of the first excited state in ^{11}Be, which we will denote as Ψ_1. The transition amplitude (a_{01}) is therefore given by :

$$
\begin{aligned}
a_{01} &= \int \Psi(\mathbf{r})^* \Psi_1 d\tau \\
&= -\int \delta\Psi_0^* \Psi_1 d\tau
\end{aligned}
\tag{D.3}
$$

Where we used the orthogonality of Ψ_0 and Ψ_1 in the last step, and ignore the spin for now.

It is a good approximation for a narrow reaction zone to replace the wave functions in the above integrand by their value $\Psi_{0,1}(b, 0, z)$ along the target trajectory. The integral over the x-y dimensions can then be done easily and leads to a factor of πR_a^2,
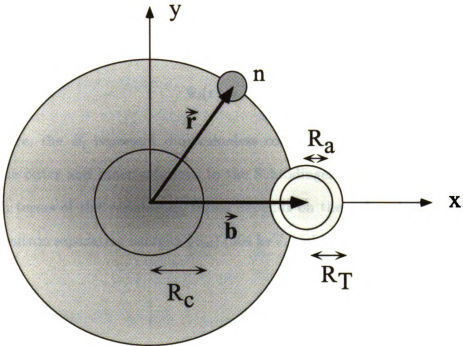
Figure D.1: The coordinate center originates in the ^{10}Be core with the radius R_C, and the relative coordinate of the halo neutron is given by $\vec{r}$. The impact parameter of the target nucleus, moving along the z axis is given by $\vec{b}$.

which is half of the (free) nucleon reaction cross section. Therefore, we can write the transition amplitude as :

$$a_{01} = -\pi R_a^2 \int \Psi_0^*(b, 0, z)\Psi_1(b, 0, z)dz \qquad (D.4)$$

This integral can be integrated numerically using Woods-Saxon wave functions. However, as the minimum impact parameter is larger than the sum of the core and target radius, the Woods-Saxon wave functions are given by the spherical Hankel functions (h_l), which represent the asymptotic behaviour of the wave functions. Therefore, we can write :

$$\Psi_l(\mathbf{r}) = B_l \kappa_l^{3/2} h_l(i\kappa_l r) Y_{lm}(\theta\phi) \qquad (D.5)$$

Here, the B_l represent dimensionless constants of the order unity, used to adjust the outer and inner solutions to the Schrödinger equation. The equation is written in terms of the variable κ_l, which depends on the reduced mass (μ) and the known neutron separation energies (S_{nl}) (504 keV, and 188 keV respectively), via the relation:

$$\kappa_l = \frac{1}{\hbar}\sqrt{2\mu S_{nl}} \qquad (D.6)$$

The lowest order Hankel functions are given by :

$$h_0(i\kappa_0 r) = -\frac{1}{\kappa_0 r}e^{-\kappa_0 r} \qquad (D.7)$$

$$h_1(i\kappa_1 r) = i\left(\frac{1}{\kappa_1 r} + \frac{1}{\kappa_1^2 r^2}\right)e^{-\kappa_1 r} \qquad (D.8)$$

One can now express the transition amplitude as :

$$a_{01} = -\pi R_a^2 B_0 B_1 \kappa_0^{3/2} \kappa_1^{3/2} \int_{-\infty}^{\infty} h_o^*(i\kappa_0 r) Y_{00} h_1(i\kappa_1 r) Y_{1m}(\theta, \phi) dz \qquad (D.9)$$

The spherical harmonics Y_{lm} are given by :

$$Y_{00} = \frac{1}{4\pi}$$

$$Y_{10} = \sqrt{\frac{3}{4\pi}} cos\theta = \sqrt{\frac{3}{4\pi}} \frac{z}{\sqrt{b^2+z^2}} \qquad (D.10)$$

$$Y_{1\pm1} = \mp\sqrt{\frac{3}{8\pi}} sin\theta \cdot e^{im\phi} = \mp\sqrt{\frac{3}{8\pi}} \frac{b}{\sqrt{b^2+z^2}}$$

Where the phase factor $e^{im\phi}$ for the $Y_{1\pm1}$ is equal to one as in the chosen coordinate system $\phi = 0$. Substituting this into equation D.9 gives :

$$a_{01} = \pi R_a^2 B_0 B_1 (\kappa_0 \kappa_1)^{3/2} \frac{\sqrt{3}}{4\pi} \int_{-\infty}^{\infty} \frac{i}{\kappa_0 r} e^{-\kappa_0 r} \left(\frac{1}{\kappa_1 r} + \frac{1}{\kappa_1^2 r^2} \right) e^{-\kappa_1 r}$$

$$\cdot \left\{ \begin{array}{ll} \frac{z}{\sqrt{b^2+z^2}} dz & \text{for } lm = 01 \\ \mp\frac{1}{\sqrt{2}} \frac{b}{\sqrt{b^2+z^2}} dz & \text{for } lm = 0 \pm 1 \end{array} \right\} \qquad (D.11)$$

As $r = \sqrt{b^2 + z^2}$, the first integrand – the solution to the Y_{10} part – vanishes as it is odd. Therefore, we end up with :

$$a_{01} = \mp 2\pi R_a^2 B_0 B_1 b (\kappa_0 \kappa_1)^{3/2} \sqrt{\frac{3}{2}} \frac{i}{4\pi} \int_0^{\infty} \frac{e^{-(\kappa_0+\kappa_1)r}}{\kappa_0 \kappa_1 r^3} \left(1 + \frac{1}{\kappa_1 r} \right) dz \qquad (D.12)$$

We can simplify this formula even further, by identifying $2\pi R_a$ with the total neutron cross section σ_{tot}, and substitute $z = bv$ in the above integral. This leads to the

following result :

$$a_{01} = \mp\sqrt{\frac{3}{2}}\frac{iB_0B_1\sigma_{tot}\sqrt{\kappa_0\kappa_1}}{4\pi b}\left[\int_0^\infty \frac{e^{-\alpha\sqrt{1+v^2}}}{(1+v^2)^{3/2}}dv + \frac{1}{\kappa_1 B}\int_0^\infty \frac{e^{-\alpha\sqrt{1+v^2}}}{(1+v^2)^2}dv\right]$$

$$= \mp\sqrt{\frac{3}{2}}\frac{iB_0B_1\sigma_{tot}\sqrt{\kappa_0\kappa_1}}{4\pi b}\left[D\left(\frac{3}{2},\alpha\right) + \frac{1}{\kappa_1 b}D(2,\alpha)\right] \tag{D.13}$$

Where we used the following substitutions :

$$\alpha = (\kappa_0 + \kappa_1)\cdot b \tag{D.14}$$

$$D(p,\alpha) = \int_0^{-\infty} \frac{e^{-\alpha\sqrt{1+v^2}}}{(1+v^2)^p}dv \tag{D.15}$$

And the functions $D(p,\alpha)$ need to be evaluated numerically.

The transition amplitude a_{01} is related to the transition probability P_{if} via the relation :

$$P_{if} = \frac{2}{3}|a_{01}|^2 \tag{D.16}$$

where the factor $\frac{2}{3}$ comes from taking appropriate care of the spins involved. From the transition probability one can calculate the cross section via :

$$\sigma_{if} = \int_{b_{min}}^\infty P_{if}(b)2\pi b\, db$$

$$= \frac{B_0^2 B_1^2 \sigma_{tot}^2 \kappa_0\kappa_1}{8\pi}\int_{b_{min}}^{b_{max}}\left(D(\frac{3}{2},\alpha) + \frac{1}{\kappa_1 b}D(2,\alpha)\right)^2 \frac{db}{b} \tag{D.17}$$

Where the integral is over the impact parameter b, and it can be evaluated numerically. The numerical calculation gives the nuclear contribution of exciting the $\frac{1}{2}^-$ first excited state in ^{11}Be from the $\frac{1}{2}^+$ ground state, as discussed in section 3.3.2.

Bibliography

[Ann94] R. Anne, R. Bimbot, S. Dogny, H. Emling, D. Guillemaud-Mueller, P.G. Hansen, P. Hornshoj, F. Humbert, B. Jonson, M. Keim, M. Lewitowicz, P. Moller, A.C. Mueller, R. Neugart, T. Nilsson, G. Nyman, F. Pougheon, K. Riisager, M.-G. Saint-Laurent, G. Schrieder, O. Sorlin, O. Tengblad, K. Wilhelmsen Rolander, Nucl. Phys. **A575** 125 (1994).

[Ann95] R. Anne, D. Bazin, R. Bimbot, M.J.G. Borge, J.M. Corre, S. Dogny, H. Emling, D. Guillemaud-Mueller, P.G. Hansen, P. Hornshoj, P. Jensen, B. Jonson, M. Lewitowicz, A.C. Mueller, R. Neugart, T. Nilsson, G. Nyman, F. Pougheon, M.G. Saint-Laurent, G. Schrieder, O. Sorlin, O. Tengblad, K. Wilhelmsen-Rolander, Z. Phys. **A352** 397 (1995).

[Aud93] G. Audi, and A.H. Wapstra, Nucl. Phys. **A565** 1 (1993).

[Baz97] D. Bazin, to be published.

[Ber81] G.F. Bertsch, Phys. Rev. Lett. **46** 472 (1981).

[Ber95] C.A. Bertulani, L.F. Canto, M.S. Hussein, Phys. Lett. **B353** 413 (1995).

[Bro88] B.A. Brown, W.A. Richter, R.E. Julies and B.H. Wildenthal, Ann. Phys. **182** 191 (1988).

[Duf86] J.P. Dufour, R. Del Moral, H. Emmermann, F. Hubert, D. Jean, C.Poinot, M.S. Provikoff, A. Fleury, H. Delagrange, and K.-H. Schmidt, Nucl. Instr. Methods **A248** 267 (1986).

[Esb94] H. Esbensen, private communication (1994).

[Fau92] M. Fauerbach, Diploma thesis, TH Darmstadt (1992).

[Fir96] Table of Isotopes, edited by R.B. Firestone and V.S. Shirley (John Wiley and Sons, Inc, 1996), Vol. II, p. G1.

[Fox89] R. Fox, R. Au, and A. VanderMolen, IEEE Trans. Nucl. Sci. 1562 (1989).

[Fri83] W.A. Friedmann, Phys. Rev. **C27** 569 (1983).

[Gan90] H.H. Gann, S.J. Lee, S. Das Gupta, J. Barrette, Phys. Lett. **B234** 4 (1990).

[Gei95] H. Geissel, G. Münzenberg, and K. Riisager, Ann. Rev. Nucl. Part.Sci. **45** 163 (1995).

[Gla97] T. Glasmacher, P. Thirolf, and H. Scheit, to be published.

[Gol74] A.S. Goldhaber, Phys. Lett. **B53** 306 (1974).

[Gui90] D. Guillemaud-Mueller, J.C. Jacmart, E. Kashy, A. Latimier, A.C. Mueller, F. Pougheon, A. Richard, Yu.E. Penionzhkevich, A.G. Arthuk, A.V. Belozyorov, S.M Lukyanov, R. Anne, P. Bricault, C. Détraz, M. Lewitowicz, Y. Zhang, Yu.S. Lyutostansky, M.V. Zverev, D. Bazin, and W.D. Schmidt-Ott, Phys. Rev. **C41** 937 (1990).

[Han95] P.G. Hansen, A.S. Jensen, and B. Jonson, Ann. Rev. Nucl. Part.Sci. **45** 591 (1995).

[Han96] P.G. Hansen, Phys. Rev. Lett. **77**, 1016 (1996).

[Han97] P.G. Hansen, private communication (1997).

[Hub89] F. Hubert, R. Bimbot, and H. Gauvin, Nucl. Instr. Meth. **B36** 357 (1989).

[Hüf81] J. Hüfner, and M.C. Nemes, Phys. Rev. **C23** 2538 (1981).

[Kid96] T. Kido, K. Yabana, and Y. Suzuki, Phys. Rev. **C53** 2296 (1996).

[Mat97] MATHEMATICA 2.2 for VAX/VMS, Copyright 1988-93 Wolfram Research, Inc.

[Mil83] D.J. Millener, J.W. Olness, and E.K. Warburton, Phys. Rev **C28** 497 (1983).

[Möl88] P. Möller and J.R. Nix, At. Data Nucl. Data Tables **39** 221 (1988).

[Mon71] E.J. Moniz, I. Sick, R.R. Whitney, J.R. Ficenec, R.D. Kephart, W.P. Trower, Phys. Rev. Lett. **26** 445 (1971).

[Mot95] T. Motobayashi, Y. Ikeda, Y. Ando, K. Ieki, M. Inoue, N. Iwasa, T. Kikuchi, M. Kurokawa, S. Moriya, S. Ogawa, H. Murakami, S. Shimoura, Y. Yanagisawa, T. Nakamura, Y. Watanabe, M. Ishihara, T. Teranishi, H. Okuno, R.F. Casten, Phys. Lett. bf B346 9 (1995).

[Mue93] A.C. Mueller and B.M. Sherrill, Ann. Rev. Nucl. Part.Sci. **43** 529 (1993).

[Mur84] M.J. Murphy, Phys. Lett. bf B135 25 (1984).

[Mye66] W.D. Myers, and W.J. Swiatecki, Nucl. Phys. **88** 1 (1966).

[Nak97] T. Nakamura, T. Motobayashi, Y. Ando, A. Mengoni, T. Nishio, H. Sakurai, S. Shimoura, T. Teranishi, Y. Yanagisawa, and M. Ishihara, submitted to Phys. Lett. B.

[Pfa95] R. Pfaff, D.J. Morrissey, M. Fauerbach, M. Hellström, J.H. Kelley, R.A. Kryger, B.M. Sherrill, M. Steiner, J.S. Winfield, J.A. Winger, and B.M. Young, Phys. Rev. **C51** 1348 (1995).

[Pfa96] R. Pfaff, Ph. D. Thesis, Michigan State University (1996).

[Ray79]   J. Raynal, Coupled Channel Code ECIS79, unpublished.

[Ren95]   Z. Ren, W. Mittig, B. Chen, Z. Ma, Phys. Rev. **C52** R20 (1995).

[Sch96]   H. Scheit, T. Glasmacher, B.A. Brown, J.A. Brown, P.D. Cottle, P.G. Hansen, R. Harkewicz, M. Hellström, R.W. Ibbotson, J.K. Jewell, K.W. Kemper, D.J. Morrissey, M. Steiner, P. Thirolf, and M. Thoennessen, Phys. Rev. Lett. **77**, 3967 (1996).

[Sch97]   H. Scheit, to be published.

[Ser47]   R. Serber, Phys. Rev. **72** 1114 (1947).

[She91]   B.M. Sherrill, D.J. Morrissey, J.A. Nolen Jr., and J.A. Winger, Nucl. Instr. Methods **B56** 1106 (1991).

[Sto70]   E. Storm and H.I. Israel, Nucl. Data Tables A7, 565 (1970).

[Süm90]   K. Sümmerer, W. Brüchle, D.J. Morrissey, M. Schädel, B. Szweryn, and Yang Weifan, Phys. Rev. **C42** 2546 (1990).

[Swa94]   D. Swan, J. Yurkon, and D.J. Morrissey, Nucl. Instrum. Methods Phys. Res. Sect. A **348** 314 (1994).

[Tan95]   I. Tanihata, Part. Nucl. Phys. (A. Faessler ed.) **35**, 505 (1995).

[Tar96]   O. Tarasov, S. Lukyanov, Yu. Oganessian, Yu. Penoinzhkevich, E. Sokol, R. Allatt, R.D. Page, A. Reed, J.C. Angelique, N.A. Orr, J.S. Winfield, R. Anne, M. Lewitowicz, A.N. Ostrowski, M.G. Saint-Laurent, W. Trinder, C. Borcea, Z. Dlouhy, C. Donzaud, S. Grevy, D. Guillemaud-Mueller, A.C. Mueller, F. Pougheon, W. Schwab, O. Sorlin, *Nuclear Physics at GANIL*, edited by M. Bex, and J. Galin (1996), p. 50.

[Typ95]   S. Typel and G. Baur, Phys. Let. **B356** 186 (1995).

[Viy79]   Y.P. Viyogi, T.J.M. Symons, P. Doll, D.E. Greiner, H.H. Heckman, D.L. Hendrie, P.J. Lindstrom, J. Mahoney, D.K. Scott, K. Van Bibber, G.D. Westfall, H. Wieman, H.J. Crawford, C. McParland, C.K. Gelbke, Phys. Rev. Lett. **42** 33 (1979).

[Wap59]   A.H. Wapstra, G.J. Nijgh, and R. van Lieshout, Nucl. Spectroscopy Tables, North-Holland Publ. Co., Amsterdam (1959).

[Wab90]   E.K. Warburton, J.A. Becker and B.A. Brown, Phys. Rev. **C41** 1147 (1990).

[Wil84]   B.H. Wildenthal, Progress in Particle and Nuclear Physics **11**, edited by D.H. Wilkinson, Pergamon, Oxford 5 (1984).

[Win92]   J.A.Winger, B.M.Sherrill, D.J.Morrissey, Nucl. Instrum. Methods Phys. Res.**B70**, 380 (1992).

[Win79]   A. Winther and K. Alder, Nucl. Phys. **A319** 518 (1979).

[Won90]   S.S.M. Wong, Introductory Nuclear Physics, xxx

[Wou88]   J.M. Wouters, R.H. Kraus, D.J. Vieira, G.W Butler, and K.E.G. Löbner,
Z. Phys. **A331** 229 (1988).

[Zwi79]   B. Zwieglinski, W. Benenson, R.G.H. Robertson, W.R. Coker, Nucl. Phys.
A315 124 (1979).